

Aliasing in Near-Field Array Ambiguity Functions: a Spatial Frequency-Domain Framework

Gilles Monnoyer, Jérôme Louveaux, Laurence Defraigne, Baptiste Sambon, Luc Vandendorpe
ICTEAM, UCLouvain, Louvain-la-Neuve (Belgium), emails : *firstname.lastname@uclouvain.be*

Abstract—Next-generation communication and localization systems increasingly rely on extremely large-scale arrays (XL-arrays), which promise unprecedented spatial resolution and new functionalities. These gains arise from their inherent operation in the near field (NF) regime, where the spherical nature of the wavefront can no longer be ignored; consequently, characterizing the ambiguity function (AF)—which amounts to the matched beam pattern—is considerably more challenging. Implementing very wide apertures with half-wavelength element spacing is costly and complex. This motivates thinning the array (removing elements), which introduces intricate aliasing structures, *i.e.*, grating lobes. Whereas prior work has addressed this challenge using approximations tailored to specific array geometries, this paper develops a general framework that reveals the fundamental origins and geometric behavior of grating lobes in NF AFs. Using a local spatial-frequency analysis of steering signals, we derive a systematic methodology to model NF grating lobes as aliasing artifacts, quantifying their structure on the AF, and providing design guidelines for XL-arrays that operate within aliasing-safe regions. We further connect our framework to established far field (FF) principles. Finally, we demonstrate the practical value of the approach by deriving closed-form expressions for aliasing-free regions in canonical uniform linear arrays (ULAs) and uniform circular arrays (UCAs).

I. INTRODUCTION

With the recent advances towards 6G telecommunication networks and next-generation localization systems, the importance of extremely large-scale arrays (XL-arrays) has risen due to the increased spatial resolution and spectral efficiency they are anticipated to provide [1], [2]. This evolution is characterized by dimensions that fundamentally modify the operating regime of arrays. Consequently, the spherical nature of the wavefronts can no longer be ignored, thereby invalidating conventional far field (FF) conditions—defined using the Fraunhofer distance—which permitted approximating the wavefront as planar. The near field (NF) regime in which XL-arrays operate enables a single array to transmit or receive steering signals that encode both range and angular information. This feature supports advanced functionalities such as high-resolution positioning or beam pointing [3], [4]. Nonetheless, the NF regime also gives rise to beam patterns with increased structural complexity, thereby complicating the analytical characterization of system performance [5]–[7].

XL-arrays can be categorized based on their structural configurations, ranging from large co-located arrays, composed of an extremely high number of densely spaced antennas, to fully distributed XL-arrays, spreading its constituting antennas to cover extremely wide areas [8]. The latter is typically encountered in cell-free multiple-input multiple-output (MIMO) sys-

tems. On the one hand, co-located XL-arrays commonly aim to meet the seminal half-wavelength antenna spacing to avoid grating lobes, a phenomenon which is well-understood in the FF regime as the undesired illuminations of multiple angles with similar power [9]. On the other hand, populating always wider arrays with half-wavelength spaced antennas leads to important challenges in terms of computational complexity and physical constraints. These limitations motivated many recent studies to focus on alternative structures (including sparse, modular, and distributed arrays) that relax this spacing requirement while maintaining the large array aperture [10]–[12]. Such designs require dealing with effects analogous to the grating lobes, but exhibiting significantly more intricate structure than their FF counterparts. Their study constitutes the scope of this paper.

Practically, this paper studies these structures as they appear in the *ambiguity function (AF)*, which is a fundamental tool to evaluate important indicators of localization performance, such as the resolution and the ambiguities [7], [13]. It is equivalent to the matched beam pattern obtained with the maximum ratio transmission (MRT) beamformer [14]. The AF evaluates the correlations between all the possible pairs of signals associated with locations observed by the array. The perfect AF theoretically draws a Dirac, being non-zero only when matching twice the same location. In practice, finite-sized arrays introduce non-orthogonality between distinct steering signals, typically resulting in AFs with oscillatory behaviors. The width of their main lobe provides information about the inherent system’s resolution, informing how far from one another two sources must be located to result in low-correlated signals. The secondary lobes generate estimation ambiguities, *i.e.*, a risk of confusion between two source locations, which, although far from one another, exhibit correlated signals.

Severe additional estimation ambiguities arise from the presence of grating lobes. Mitigating their effect is essential to reach high performance in both single- and multi-source contexts. In the FF, it is often possible to obtain closed-form expressions of the AF with an angle-distance representation of the locations. As a result, the FF grating lobes are well-understood: antenna spacing exceeding half the wavelength introduces angular repetitions. Thanks to this understanding, their presence can be dealt with by ensuring that the source’s location is restricted to an angular sector as seen by the array. Alternatively, several other techniques have been suggested in the literature to address grating lobe mitigation in the FF. In [15], a sparse MIMO system composed of several linear

subarrays transmitting at distinct frequencies is considered. The authors in [16] reduce the grating lobes by leveraging variations in subarray spacing, orientation, and density, while [17] resolves angular repetitions using a compressed sensing approach, constrained to an angular sector.

To similarly mitigate the effect of grating lobes in the NF regime, obtaining mathematical descriptions of their geometrical structure in the AF is crucial. This task is particularly challenging because the NF introduces additional complexities due to the nonlinear spatial phase variations in steering signals, rendering exact closed-form expressions of the AFs generally unobtainable. Recent approaches have largely relied on angle-distance domain analysis, leveraging *simplifying assumptions* to obtain approximate closed-form expressions of the AF for specific array topologies. For example, the authors in [1] exploit the unique regular structure of modular XL-arrays and define a sub-array-based uniform spherical wave model that assumes an inner FF regime within each module. In [12], the achievable beamwidth that maintains a low grating lobes level is investigated in a similar modular XL-array context. Additionally, [11] exploits Fresnel approximations to evaluate the beam patterns for linear sparse arrays and extended coprime arrays.

While these approaches provide valuable insights, they rely on context-specific simplifications that limit their generality. Moreover, they exploit definitions of NF grating lobes that heuristically extend that of their FF counterparts, inherently lacking a formal theoretical foundation in the NF. Indeed, the FF grating lobes are characterized by three *equivalent* definitions:

- 1) Secondary lobes with the same amplitude as the main lobe.
- 2) The effect of pairs of distinct locations (or angles) producing identical steering signals (up to a phase constant).
- 3) The effect of locations yielding signals affected by spatial aliasing.

In the NF, the first two definitions rarely (and presumably never) occur because the NF's non-linear phase structure prevents exact repetitions of steering signals. This is observed in [1], [8], [18] and in the AFs numerically computed in our paper. In contrast, defining the grating lobes as spatial *aliasing artifacts* remains formally valid in the NF regime. By building our analysis upon this definition, we define a framework that is both theoretically grounded in the structural origins of grating lobes and directly consistent with established FF conventions.

Our novel framework offers the key advantage of determining grating lobe properties without requiring the challenging derivation of closed-form expressions for the AF. Exploiting a *spatial frequency-domain* representation of signals, we are able to track the set of locations that generates the spectral folding associated with visible grating lobes in the AF. Moreover, the abstract geometric formulation of our methodology enables its applicability to a wide range of various array topologies.

Practically, our framework therefore supports the systematic design of NF XL-array systems that operate safely with respect to grating lobes. Indeed, once the structure of aliasing effects is understood, antenna locations and spacings can be linked to a region of aliasing-free positions. Building on this principle, our

paper departs from prior studies and proposes the theoretical construction of aliasing-safe operational areas for XL-arrays.

To construct this new framework, we compressively capture the spatial spectral content of steering signals by exploiting the concept of *local* spatial frequencies. These have already been formalized in multiple studies conducted in the context of channel degrees of freedom [19]–[21]. Similarly, NF steering signals can be interpreted as *spatial chirp*. This concept, notably reported in [22]–[24], aligns with the standard instantaneous frequency representation of chirps in the time domain.

This paper, therefore, extends the preliminary findings of [25] and proposes a systematic methodology to characterize the complex grating lobe structure that arises in the AF of XL-arrays operating in the NF regime. We also deduce practical design guidelines for XL-arrays. Using a local spatial frequency (or “chirp-based”) representation of steering signals, we link our framework to known results in the FF regime.

Consequently, the contributions of this paper are:

- A mathematical formalism defining the NF grating lobes as effects of “aliasing artifacts”;
- A novel framework enabling the systematic mathematical description of the geometry drawn by these aliasing artifacts on the AF;
- Practical guidelines for designing arrays operating in aliasing-safe areas;
- A chirp-based compressive modeling of the steering signal’s spectrum that connects our NF conclusions with seminal results known for the FF;
- Interpretable closed-form expressions describing the complex grating lobes structures in canonical uniform linear arrays (ULAs) and uniform circular arrays (UCAs).

The remainder of this paper is organized as follows. In Section II, we establish the theoretical model that constitutes the focus of this paper. Section III formalizes the concept of AF’s aliasing effect, and presents our framework to understand their structure. Next, Section IV extends our findings using a local spatial spectral modeling that connects it with known FF principles. The practical guidelines that originate from our framework follow in Section IV-B. Finally, Sections V and VI apply our theoretical framework, respectively, to specific ULA and UCA topologies, providing closed-form expressions that explain the grating lobes’ structure.

Mathematical Notations

In the current paper, the imaginary unit is $j = \sqrt{-1}$ and c is the speed of light. The operator \otimes denotes the convolution product. The symbol $;$ separating inputs in functions, as $f(x; y)$, indicates its functional dependence on the variable x and parameterization by y . Bold lowercase letters denote vectors, and caligraphic-style uppercase letters, like \mathcal{P} , are sets. The notations $\|\mathbf{a}\|$ and $\angle \mathbf{a}$ respectively are the ℓ_2 -norm and the angle of the vector \mathbf{a} . Given the vector \mathbf{a} and the scalar factor b , the set $b \cdot \mathcal{P} + \mathbf{a}$ is identical to \mathcal{P} but rescaled by b and translated by \mathbf{a} .

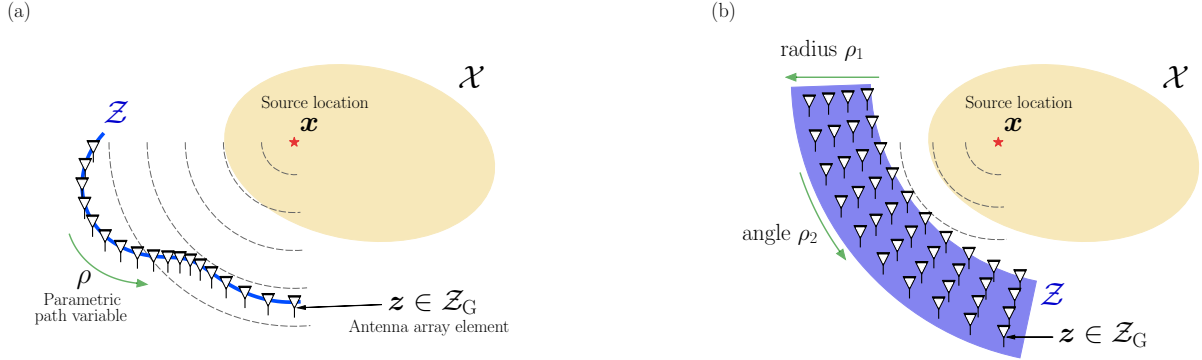


Fig. 1. Schematic representation of the uplink scenario studied in this paper. (a) A case where the antenna array is defined over a curve \mathbf{z} parameterized by a scalar path variable ρ . (b) A case where the antenna array is parameterized with two path variables. Representation of the simple case of the polar description.

II. SYSTEM MODEL

The content of this paper is formulated for a canonical uplink scenario where a static user equipment (UE), located in \mathbf{x} , transmits a unit-energy baseband signal $s(t)$ modulated around the carrier having a frequency f_c . As illustrated in Figure 1, the transmitted signal is captured by an XL-array. The antennas are located in the grid \mathcal{Z}_G that discretizes the continuous-space domain \mathcal{Z} . Note that our system model allows \mathcal{Z}_G to represent *any* discrete subset of \mathcal{Z} , and is therefore not restricted to uniform planar grids. This array aims to perform network-based positioning, given a source location \mathbf{x} , known to be taken from an *operating domain* $\mathcal{X} \subseteq \mathbb{R}^d$.

Following physical optics principles, the antenna array element (AAE) located in $\mathbf{z} \in \mathcal{Z}$ measures, up to an additive white gaussian noise (AWGN), the baseband equivalent signal

$$s_R(t, \mathbf{z}; \mathbf{x}) = \frac{e^{-jk_c \|\mathbf{z} - \mathbf{x}\|}}{\|\mathbf{z} - \mathbf{x}\|} s\left(t - \frac{\|\mathbf{z} - \mathbf{x}\|}{c}\right), \quad (1)$$

where $k_c = 2\pi f_c/c = 2\pi/\lambda_c$.

To simplify mathematical developments, we use a normalized formulation with respect to the total received energy

$$\mathcal{E}(\mathbf{x}) = \int_{\mathcal{Z}} \|\mathbf{z} - \mathbf{x}\|^{-2} d\mathbf{z}. \quad (2)$$

Using the above, we can now write

$$s_R(t, \mathbf{z}; \mathbf{x}) = \mathcal{E}^{\frac{1}{2}}(\mathbf{x}) h(\mathbf{z}; \mathbf{x}) s\left(t - \frac{\|\mathbf{z} - \mathbf{x}\|}{c}\right), \quad (3)$$

where the wave propagation coefficients, or the *steering signal*,

$$h(\mathbf{z}; \mathbf{x}) = a(\mathbf{z}; \mathbf{x}) \exp(-j\phi(\mathbf{z}; \mathbf{x})), \quad (4)$$

provides the energy-normalized phase and attenuation received at the antenna located in position \mathbf{z} , parameterized by the given source location \mathbf{x} , with

$$\phi(\mathbf{z}; \mathbf{x}) = k_c \|\mathbf{z} - \mathbf{x}\|, \quad (5)$$

$$a(\mathbf{z}; \mathbf{x}) = (\mathcal{E}^{\frac{1}{2}}(\mathbf{x}) \|\mathbf{z} - \mathbf{x}\|)^{-1}. \quad (6)$$

By definition, the steering signal $h(\mathbf{z}; \mathbf{x})$ thus exhibits unit energy regardless of the value of \mathbf{x} .

The current paper assumes a narrowband signal $s(t)$, restricting our focus to the wave propagation coefficients described by $h(\mathbf{z}; \mathbf{x})$. We postpone the interplay with wideband aspects and the extension to moving targets to future work.

In the NF regime, the phase $\phi(\mathbf{z}; \mathbf{x})$ is *non-linear* along \mathbf{z} , enabling beam pointing at a single location. While the *continuous-space* steering signal $h(\mathbf{z}; \mathbf{x})$ ensures such focusing, its *discrete-space* counterpart, obtained from the finite set of antennas in \mathcal{Z}_G , may introduce grating lobes causing localization ambiguities. Conventional FF interpretations of the grating lobes do not apply in the NF, as they ignore this non-linear phase structure, a gap our framework addresses in the following sections.

Parametric representation

In this paper, we adopt a general parametric model based on a transformation function, denoted by ν , that defines a *bijection* between a compact parametric domain $\mathcal{P} \in \mathbb{R}^q$ and the antenna domain \mathcal{Z} . It directly results

$$\mathcal{Z} = \{\nu(\rho) : \rho \in \mathcal{P}\}. \quad (7)$$

For example, Figure 1a shows a 1D-curved \mathcal{Z} parameterized by the path variable ρ , and Figure 1b shows another case where ρ is a polar description of \mathbf{z} . This artifice enables us to

- (i) easily encapsulate many possible topologies in a single framework, notably including canonical ULAs, UCAs, and paving the way for more complex structures,
- (ii) assume only uniform Cartesian sampling of the parametric domain \mathcal{P} , denoted by \mathcal{P}_G , without loss of generality on the definition of \mathcal{Z}_G .

Any desired grid \mathcal{Z}_G can be obtained from a uniform Cartesian grid \mathcal{P}_G using a bijection operator ν , thereby maintaining the generality of our approach. This allows us to analyze grating lobes originating from any set of locations \mathcal{Z}_G using standard Fourier theory on \mathcal{P}_G .

For the readability of the current paper, we express our results only for $q = 1$, as represented in Figure 1a, with Δ denoting the sampling step generating \mathcal{P}_G from \mathcal{P} . The extension to $q > 1$ can be obtained by following the steps of this paper with multi-dimensional Fourier transforms, in which the spectral folding must be considered separately in each dimension.

Replacing $\mathbf{z} = \nu(\rho)$ in the steering signal model, we thus focus on the signal $h(\nu(\rho); \mathbf{x})$ as a function of ρ .

III. ALIASING ARTIFACTS IN THE AMBIGUITY FUNCTION

This section defines the AF for the NF sensing context described in Section II, and establishes a formalism to characterize the sophisticated NF grating lobes as the result of an aliasing process.

To clarify our methodology, the quantities we present throughout this section are illustrated with a toy example composed of a horizontal ULA of length $1000\lambda_c$ centered in $\mathbf{0}$. Defining the trivial transformation $\nu_{\text{toy}}(\rho) := [\rho, 0]^\top$, we build the grid \mathcal{Z}_G by taking values of ρ in the uniform grid \mathcal{P}_G with a spacing $\Delta = 10\lambda_c$. For example, with a high carrier frequency $f_c = 60\text{GHz}$, this corresponds to a co-located 5m-long linear array with a 5cm antenna spacing. Alternatively, at a lower carrier frequency $f_c = 200\text{MHz}$, it can also correspond to a *distributed* array composed of 100 access points spaced 15m apart. We fix the user location in $\mathbf{x} = [0, 600\lambda_c]$, centered in front of the array, in its NF operational region.

A. Near-field ambiguity functions

The AF is an important tool used to evaluate the structural properties of a sensing system. Motivated by a maximum likelihood estimation approach in the presence of AWGN, it is defined as the noise-free matched-filter response of the sensing system for a *tested* position $\tilde{\mathbf{x}}$, while the *true* source's position is \mathbf{x} . For the system defined in Section II, its standard expression in a *wideband* context is

$$\mathcal{A}(\tilde{\mathbf{x}}, \mathbf{x}) := \sum_{\mathbf{z} \in \mathcal{Z}_G} \int_{-\infty}^{\infty} \bar{s}^*(t, \mathbf{z}; \tilde{\mathbf{x}}) \bar{s}(t, \mathbf{z}; \mathbf{x}) dt, \quad (8)$$

where $\bar{s}(t, \mathbf{z}; \mathbf{x}) = \mathcal{E}^{-\frac{1}{2}}(\mathbf{x})s(t, \mathbf{z}; \mathbf{x})$.

In practice, the AF is inherently tied to the probability of erroneously detecting $\tilde{\mathbf{x}}$ instead of the true location \mathbf{x} . When multiple sources must be located, it also informs on the mutual interference between the signals received from the different sources. A higher value of $\mathcal{A}(\tilde{\mathbf{x}}, \mathbf{x})$ indicates a higher probability of failing to distinguish two sources respectively located in $\tilde{\mathbf{x}}$ and \mathbf{x} . This situation typically arises, by definition, when $\tilde{\mathbf{x}}$ and \mathbf{x} are closer than the array's resolution. However, the grating lobes reveal pairs of *further apart* locations that can also be unresolvable. This emphasizes the need to study their properties.

In the narrowband settings of this paper, the AF reduces to the correlation function between possible pairs of steering signals, providing the theoretical signature of the antenna array. When associated with the measurement of the continuous steering signal, it yields

$$\mathcal{A}(\tilde{\mathbf{x}}, \mathbf{x}) := \int_{\mathcal{P}} g(\rho; \tilde{\mathbf{x}}, \mathbf{x}) d\rho, \quad (9)$$

where we define the *matched signal* as

$$g(\rho; \tilde{\mathbf{x}}, \mathbf{x}) := h^*(\nu(\rho); \tilde{\mathbf{x}}) h(\nu(\rho); \mathbf{x}), \quad (10)$$

for the simplicity of the notations throughout this section. Considering now the discrete-space steering signal, observed by the antennas in \mathcal{Z}_G , we define the discrete-space AF

$$\mathcal{A}_S(\tilde{\mathbf{x}}, \mathbf{x}) := \Delta \sum_{\rho \in \mathcal{P}_G} g(\rho; \tilde{\mathbf{x}}, \mathbf{x}). \quad (11)$$

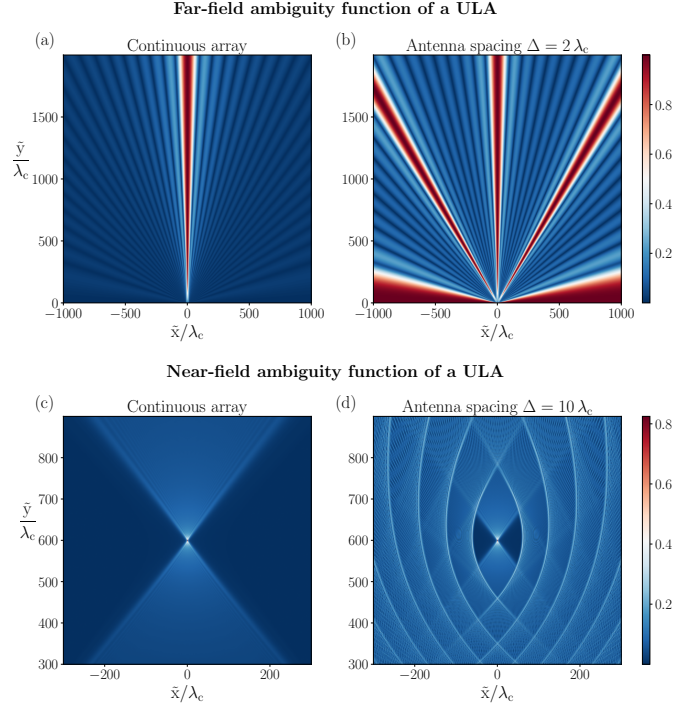


Fig. 2. Ambiguity functions for (top) a horizontal ULA with length $20\lambda_c$ operating in the FF, and (bottom) the ULA from our toy example in the NF, as a function of $\tilde{\mathbf{x}} = [\tilde{x}, \tilde{y}]^\top$ given the fixed location $\mathbf{x} = [x, y] = [0, 600]\lambda_c$. It shows in (a)-(c) the continuous-space $|\mathcal{A}(\tilde{\mathbf{x}}, \mathbf{x})|$ and in (b)-(d) the discrete-space $|\mathcal{A}_S(\tilde{\mathbf{x}}, \mathbf{x})|$, with Δ chosen for improved visibility of the grating lobes.

The AF behaves differently in the FF and NF regimes. Figure 2 illustrates this contrast by showing continuous- and discrete-space AFs for ULAs operating in both contexts. Compared to its FF counterpart, the NF AF offers a high resolution in both angle and range, enabling beam pointing and highlighting a potential superiority of XL-arrays [5], [12].

With the large antenna spacing used to generate this figure, the discrete-space AFs display grating lobes. Their well-understood angular structure in the FF regime appears in Figure 2b, whereas Figure 2d shows the more sophisticated geometry exhibited in the NF case. By developing on the *aliasing* nature of the NF grating lobes, this paper mathematically characterizes their origin and their intricate geometrical structure. Although the resolutions of the main lobe and the grating lobes are additional important factors affecting both localization and communication performance, extending our framework to include this aspect is left for future studies.

We finally highlight the mathematical connection between the narrowband AF and the concept of beam pattern commonly used to study the performance of communication systems. The beam pattern is classically defined as the set of correlations between each steering vector and a *generic* beamformer, *i.e.*, one not restricted to the set of steering vectors. As discussed in [14], the AF in (11) corresponds precisely to the beam pattern obtained with beamforming weights tailored for the specific MRT/maximum ratio combining (MRC) strategy.

B. Aliasing artifacts

This section develops the resulting spectral folding process that generates “aliasing artifacts” in $A_S(\tilde{\mathbf{x}}, \mathbf{x})$, formally defining these NF grating lobes. To this end, we exploit the conditions that yield equality between the sum (9) and the integral (11). Such conditions arise by observing that (9) amounts to evaluating the Fourier transform (FT), $G(\omega; \tilde{\mathbf{x}}, \mathbf{x})$, of the matched signal $g(\rho; \tilde{\mathbf{x}}, \mathbf{x})$ for $\omega = 0$. Indeed, given that

$$G(\omega; \tilde{\mathbf{x}}, \mathbf{x}) = \int_{\mathcal{P}} g(\rho; \tilde{\mathbf{x}}, \mathbf{x}) e^{-j\omega\rho} d\rho, \quad (12)$$

we have

$$A(\tilde{\mathbf{x}}, \mathbf{x}) = G(0; \tilde{\mathbf{x}}, \mathbf{x}). \quad (13)$$

Figure 3a shows the spectra $G(\omega; \tilde{\mathbf{x}}, \mathbf{x})$ obtained in the context of our toy example, for multiple tested locations $\tilde{\mathbf{x}}$. The reference spectrum obtained when $\tilde{\mathbf{x}} = \mathbf{x}$ exhibits a strong unit-height peak in $\omega = 0$, yielding $A(\mathbf{x}, \mathbf{x}) = 1$. As $\tilde{\mathbf{x}}$ becomes further away from \mathbf{x} , the spectral energy in $G(\omega; \tilde{\mathbf{x}}, \mathbf{x})$ is both frequency-spread and shifted, lowering its value in $\omega = 0$ and hence the value of $A(\tilde{\mathbf{x}}, \mathbf{x})$.

Let us now analyze the discrete-space AF given in (11). It is similarly equivalent to the FT of the discretized matched signal, in $\omega = 0$. Uniformly sampling g causes repetitions in its spectrum, which directly lead to

$$A_S(\tilde{\mathbf{x}}, \mathbf{x}) = \sum_{p \in \mathbb{Z}} G\left(\frac{2\pi p}{\Delta}; \tilde{\mathbf{x}}, \mathbf{x}\right) \quad (14)$$

$$= A(\tilde{\mathbf{x}}, \mathbf{x}) + \sum_{p \in \mathbb{Z} \setminus \{0\}} G\left(\frac{2\pi p}{\Delta}; \tilde{\mathbf{x}}, \mathbf{x}\right). \quad (15)$$

The right-side summation of (15) isolates the aliasing artifacts affecting the discrete-space AF, $A_S(\tilde{\mathbf{x}}, \mathbf{x})$, compared to the continuous-space reference $A(\tilde{\mathbf{x}}, \mathbf{x})$. These aliasing terms are strictly zero when the spectrum $G(\omega; \tilde{\mathbf{x}}, \mathbf{x})$ spans over frequencies that are lower, in absolute value, than the sampling frequency $2\pi/\Delta$. This observation is similar to the Shannon-Nyquist sampling theorem, but is relaxed by a factor of 2. This factor stems from the specificity that aliasing artifacts appear in $A_S(\tilde{\mathbf{x}}, \mathbf{x})$ only when spectral folding affects G in $\omega = 0$. Potential folding altering this spectrum in any other frequency has no consequence on the discrete-space AF.

Formally, defining the maximum frequency content, coined the “strict band limit”, of the matched signal $g(\rho; \tilde{\mathbf{x}}, \mathbf{x})$, as

$$\bar{K}_0(\tilde{\mathbf{x}}, \mathbf{x}) = \max\{|\omega| : |G(\omega; \tilde{\mathbf{x}}, \mathbf{x})| > 0\}, \quad (16)$$

this *sufficient* condition is given in Lemma 1.

Lemma 1. *Given a pair of locations $\tilde{\mathbf{x}}$ and \mathbf{x} , if the band limit satisfies*

$$\bar{K}_0(\tilde{\mathbf{x}}, \mathbf{x}) \leq 2\pi\Delta^{-1}, \quad (17)$$

then the equality $A_S(\tilde{\mathbf{x}}, \mathbf{x}) = A(\tilde{\mathbf{x}}, \mathbf{x})$ holds.

Proof. By construction of (16), the condition (17) directly nullifies all the terms in the right-side summation of (15). \square

Reciprocally, given the true source location \mathbf{x} , aliasing artifacts can appear in the discrete-space AF for the values of $\tilde{\mathbf{x}}$ that do *not* satisfy (17). As a result, Lemma 1 is the key

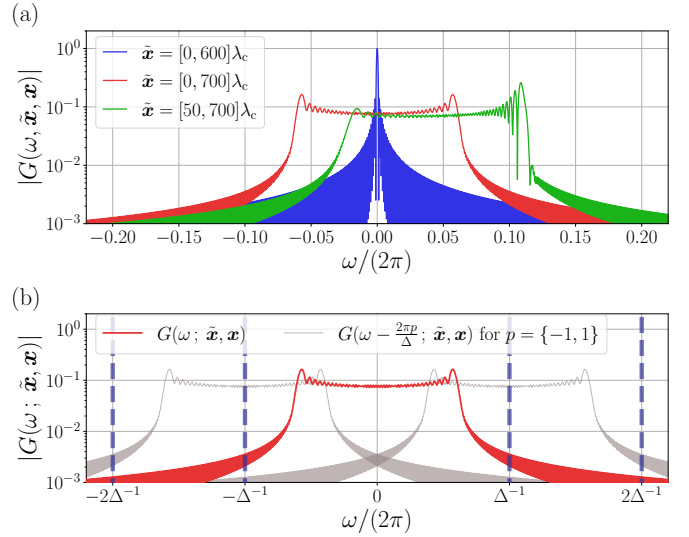


Fig. 3. Matched spectrum’s amplitude $|G(\omega; \tilde{\mathbf{x}}, \mathbf{x})|$ corresponding to the toy example for multiple tested locations $\tilde{\mathbf{x}}$, given $\mathbf{x} = [0, 600]\lambda_c$.

to determining the set of $\tilde{\mathbf{x}}, \mathbf{x}$ that are unaffected by grating lobes in $A_S(\tilde{\mathbf{x}}, \mathbf{x})$.

However, we emphasize that, in practice, the above formulation of Lemma 1 is unusable. Indeed, as exemplified in Figure 3, the strict band limit $\bar{K}_0(\tilde{\mathbf{x}}, \mathbf{x})$ typically yields infinity. A common practice is to instead define the band limit in a *soft* manner, using a small tolerance threshold ϵ rather than a strict zero in (16). Yet, this intuitive approach lacks consistency to define a framework that connects with established FF conventions, and is sensitive to the choice of ϵ . As detailed in Section IV, we address this matter by introducing a chirp-based compressive representation of the spectral content of $G(\omega; \tilde{\mathbf{x}}, \mathbf{x})$, bridging our NF framework with the classical FF interpretation of grating lobes, and leading to design guidelines for XL-arrays.

Figure 3b illustrates the repetitions affecting the spectrum, obtained for $\tilde{\mathbf{x}} = [0, 700]\lambda_c$, at every multiple of $\frac{2\pi p}{\Delta}$. Although we observe significant spectral folding in some part of the spectrum, the zero-frequency is barely folded, resulting in no visible artifacts in the discrete-space AF in $\tilde{\mathbf{x}} = [0, 700]\lambda_c$ (see Figure 2b). An intuitive representation of Lemma 1 is as follows: if the spectrum’s “significant” support remains entirely within the $\frac{2\pi}{\Delta}$ dashed line displayed in Figure 3b, then the discrete-space AF is aliasing-free at the value $\tilde{\mathbf{x}}$ that generated the observed spectrum. It is therefore important to understand that outside the specific FF case, the AF itself is *not* directly repeated by the sampling of g . Instead, the geometry of the artifacts altering $A_S(\tilde{\mathbf{x}}, \mathbf{x})$ is dictated, in each direction around \mathbf{x} , by the spread and shift behaviours of G toward the folding boundaries as $\tilde{\mathbf{x}}$ moves away from \mathbf{x} .

By observing the spectra in Figure 3, we note that the extremities of their band exhibit sharp peaks that are a few dB higher than the bands’ centers. When $\tilde{\mathbf{x}}$ reaches a value such that this peak crosses the $\frac{2\pi}{\Delta}$ critical point, a strong aliasing front appears in $A_S(\tilde{\mathbf{x}}, \mathbf{x})$. As $\tilde{\mathbf{x}}$ continues to move away from \mathbf{x} , the spectrum keeps spreading its energy, thereby lowering

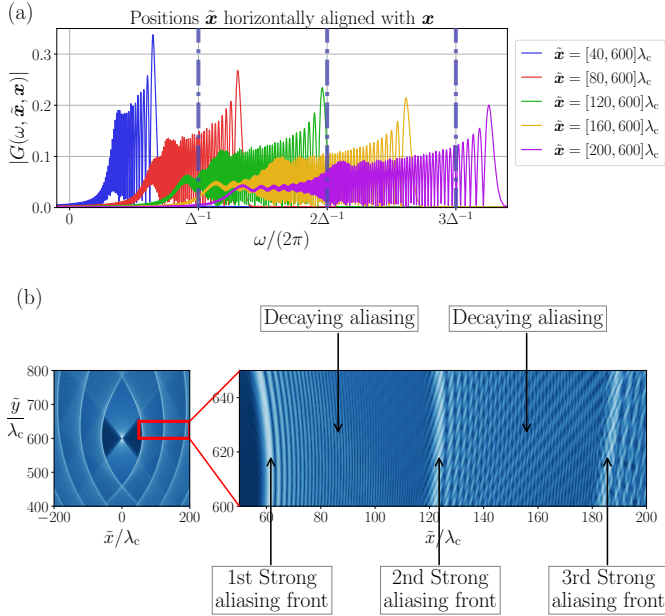


Fig. 4. Representation of the spreading of the spectrum $G(\omega; \tilde{\mathbf{x}}, \mathbf{x})$ and its effect on the discrete-space AF displayed in Figure 2. (a) Spectrum for multiple locations $\tilde{\mathbf{x}}$ given $\mathbf{x} = [0, 600]\lambda_c$. (b) Zoom in Figure 2b showing the distinct aliasing regions in the resulting discrete-space AF.

its value in $\frac{2\pi}{\Delta}$. Figure 4a shows an example of this progressive spectrum spreading. This results in a decaying strength of the aliasing artifacts as we enter deeper into the aliased region of the AF. When the spectrum spreads so much that it crosses $\frac{4\pi}{\Delta}$, a second strong aliasing front appears and then decays again. This process repeats for all $p \geq 1$ as illustrated in Figure 4b, which zooms on the aliasing patterns we observed in Figure 2b.

We note that the width of these aliasing fronts reflects the width of the prominent sharp peak in the spectra of Figure 2a. Deriving analytical expressions for these widths, however, lies beyond the scope of this study, which is focused on determining the boundaries of the aliasing-free regions.

As discussed earlier, the spectra observed in these figures illustrate the necessity to define a soft band limit that gives a practical meaning to Lemma 1. Since $|G(\omega; \tilde{\mathbf{x}}, \mathbf{x})|$ never durably reaches zero, we highlight that strictly speaking, non-zero aliasing artifacts arise under any sampling step, even finer than $\frac{\lambda_c}{2}$. This observation has already been highlighted, for example, in [26]. This principle also holds in the FF regime, where a sufficiently small sampling step that avoids grating lobes still deteriorates the theoretical cardinal sine-shaped AF into a Dirichlet kernel¹-shaped one.

Consequently, Section IV presents our approach to derive a soft definition of the band limit that enables the derivation of analytically tractable closed-form expressions in the NF regime while matching standard conventions when particularized to the FF regime.

¹A *Dirichlet kernel* denotes the $\frac{\sin(Nx)}{\sin(x)}$ function.

IV. CHIRP-BASED COMPRESSIVE SPECTRUM MODELLING

To deal with the theoretical impossibility of satisfying (17), we aim to replace its right term by a softer alternative. Instead of an intuitive ϵ -tolerant band, we leverage the theoretical findings of the authors in [27], and follow the preliminary results we elaborated in [25]. More precisely, we exploit a chirp structure representation of the matched function g to define a practical definition of the band limit. The approach of this section, therefore,

- 1) provides a compressive spectral representation of $G(\omega; \tilde{\mathbf{x}}, \mathbf{x})$;
- 2) enables *closed-form expressions* of the aliasing artifact fronts in the discrete-space AF, as exemplified in the next sections;
- 3) reduces to known results in the FF regime, hence providing a generalized framework.

A. Chirp-based analysis of aliasing artifacts

Let us define notations to separate the matched signal by its phase and amplitude as

$$g(\rho; \tilde{\mathbf{x}}, \mathbf{x}) = \alpha(\rho) \exp(-j\xi(\rho)), \quad (18)$$

where we set the amplitude and phase functions

$$\alpha(\rho) := a(\nu(\rho); \tilde{\mathbf{x}}) a(\nu(\rho); \mathbf{x}), \quad (19)$$

$$\xi(\rho) := k_c(\|\nu(\rho) - \mathbf{x}\| - \|\nu(\rho) - \tilde{\mathbf{x}}\|). \quad (20)$$

In the above, we voluntarily omitted the dependencies on $\tilde{\mathbf{x}}$ and \mathbf{x} for the sake of readability. We interpret the non-linear phase content $e^{-j\xi(\rho)}$ as a spatial “chirp”, by reference to time chirp signals that are commonly used, for example, in radar systems. Formally, a *spatial* (resp. *time*) chirp is defined by a varying *local wave number* (resp. *instantaneous frequency*). As notably seen in [19], [20], this local wave number is defined by the derivative $\xi'(\rho)$ of $\xi(\rho)$. Figure 5a plots a matched function captured in the context of the toy examples, showing its chirp nature, characterized by a slowly varying amplitude and a fast non-linear phase variation.

Assuming a high-frequency source signal (*i.e.*, a large k_c), the phase factor $e^{-j\xi(\rho)}$ oscillates much faster than $\alpha(\rho)$. This allows us to neglect the latter’s convolutive effect that widens the support of the matched spectrum, compared to the pure phase factor’s one. More precisely, given $G_\xi(\omega)$ and $G_\alpha(\omega)$ denoting the FTs of, respectively, $e^{-j\xi(\rho)}$ and $\alpha(\rho)$, we have

$$G(\omega; \tilde{\mathbf{x}}, \mathbf{x}) = \frac{1}{2\pi} G_\xi(\omega) \otimes G_\alpha(\omega). \quad (21)$$

The convolution in (21) implies that the band limit of $G(\omega; \tilde{\mathbf{x}}, \mathbf{x})$ equals that of $G_\xi(\omega)$ plus the bandwidth of $G_\alpha(\omega)$. As illustrated in Figure 5a, the typically slow variations of $a(\rho)$ (compared to λ_c) yields a narrowband spectrum $G_\alpha(\omega)$ whose bandwidth can be neglected. We thus reduce our study to the content of $G_\xi(\omega)$ as a good indication of $G(\omega; \tilde{\mathbf{x}}, \mathbf{x})$. This assumption is further supported by Figure 5b-d, showing the similarities between the complete spectrum and its sole phase factor counterpart.

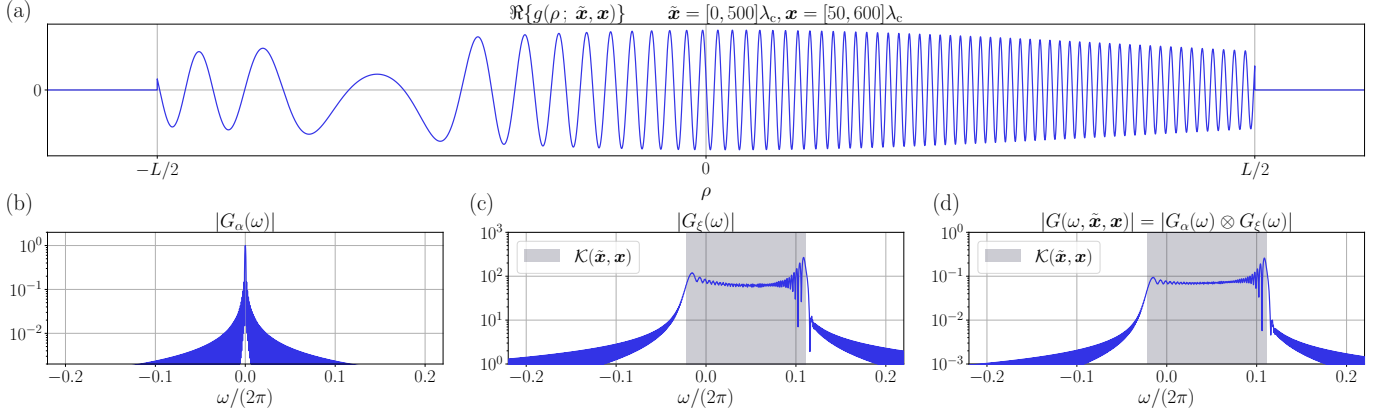


Fig. 5. Representation of the chirp-structured matched signal $g(\rho; \tilde{\mathbf{x}}, \mathbf{x})$ for $\mathbf{x} = [0, 600]\lambda_c$ and $\tilde{\mathbf{x}} = [50, 700]\lambda_c$. (a) Real part of $g(\rho; \tilde{\mathbf{x}}, \mathbf{x})$. (d) Corresponding spectrum, decomposed by (b) the amplitude's spectrum and (c) the phase factor's spectrum.

As supported by the theoretical findings detailed in [27], the set of local spatial frequencies observed by the array, defined as

$$\mathcal{K}(\tilde{\mathbf{x}}, \mathbf{x}) := \{\dot{\xi}(\rho) : \rho \in \mathcal{P}\}, \quad (22)$$

constitutes a good indication of the “most active” spatial frequency (wave number) content in the chirp’s spectrum. This has been notably formalized by the concept of “local spatial bandwidth” [19]. Capitalizing on this approach, Definition 1 provides a practical expression of the spatial band limit, which matches its significant spectral content in practical cases. Said differently, the set of local frequencies $\mathcal{K}(\tilde{\mathbf{x}}, \mathbf{x})$ yields a compressive spectral modeling of the matched signal.

Definition 1 (Soft Band Limit). *The soft band limit associated with the locations $\tilde{\mathbf{x}}$ and \mathbf{x} is the maximal local frequency of the matched signal $g(\rho; \tilde{\mathbf{x}}, \mathbf{x})$. It is thereby defined as*

$$K(\tilde{\mathbf{x}}, \mathbf{x}) := \max_{\rho \in \mathcal{P}} |\dot{\xi}(\rho)|. \quad (23)$$

Now equipped with Definition 1, we can substitute the impractical strict band limit $\bar{K}_0(\tilde{\mathbf{x}}, \mathbf{x})$ by the softer $K(\tilde{\mathbf{x}}, \mathbf{x})$ in Lemma 1. Guidelines to safely design arrays straightforwardly follow in Section IV-B.

B. Aliasing-free regions and aliasing-safe operating domain

Using the expression $K(\tilde{\mathbf{x}}, \mathbf{x})$ in Lemma 1 enables us to define a region in the discrete-space AF, $\mathcal{A}_S(\tilde{\mathbf{x}}, \mathbf{x})$, that is free of significant aliasing. This leads to Definition 2.

Definition 2 (Aliasing-Free Region). *The “aliasing-free region (AFR)” associated with the source location \mathbf{x} is the set of all the tested locations $\tilde{\mathbf{x}}$ that yield no aliasing when evaluating $\mathcal{A}_S(\tilde{\mathbf{x}}, \mathbf{x})$. Mathematically, it is expressed as*

$$\mathcal{S}(\mathbf{x}) := \{\tilde{\mathbf{x}} : K(\tilde{\mathbf{x}}, \mathbf{x}) \leq 2\pi\Delta^{-1}\}. \quad (24)$$

The aliasing front, for instance observed in Figure 2b, is given by the boundary of $\mathcal{S}(\mathbf{x})$, denoted by $\partial\mathcal{S}(\mathbf{x})$. We also note that $\partial\mathcal{S}(\mathbf{x})$ is the contour line of the function $K(\tilde{\mathbf{x}}, \mathbf{x})$ at the level $2\pi\Delta^{-1}$.

It is important to note that the aliasing-free region (AFR) is a *location-dependent* concept since each source location \mathbf{x}

leads to a possibly different AFR. By contrast, Definition 3 proposes a global concept that only depends on the structure of the array. Still, both concepts depend on the sampling step Δ , as seen in (24).

Definition 3 (Aliasing-Safe operating Domain). *The operating domain \mathcal{X} is an “aliasing-safe operating domain (ASOD)” if all the pairs $\tilde{\mathbf{x}}, \mathbf{x} \in \mathcal{X}$ yield no aliasing in $\mathcal{A}_S(\tilde{\mathbf{x}}, \mathbf{x})$. Mathematically, this is achieved if and only if, for all $\mathbf{x} \in \mathcal{X}$,*

$$\mathcal{X} \subseteq \mathcal{S}(\mathbf{x}). \quad (25)$$

We emphasize that (25) is equivalent to stating that all possible pairs of true and tested locations, $\tilde{\mathbf{x}}, \mathbf{x} \in \mathcal{X}$, are such that $\tilde{\mathbf{x}} \in \mathcal{S}(\mathbf{x})$. Under this condition, no grating lobe ever appears in the AF restricted to \mathcal{X} . We also note that ASODs are typically not unique for a given spacing Δ .

These definitions lead to design guidelines to avoid estimation ambiguities over a targeted operating domain \mathcal{X} .

- 1) For a given array geometry \mathcal{Z} , obtain the soft spatial band limit $K(\tilde{\mathbf{x}}, \mathbf{x})$.
- 2) Derive the AFR $\mathcal{S}(\mathbf{x})$ as a function of both \mathbf{x} and the spacing Δ .
- 3) Using Definition 3, derive the value of Δ required to ensure that the domain \mathcal{X} is an ASOD, *i.e.*, meets (25).

Whereas steps 1) and 2) are analytical, step 3) likely requires the development of dedicated numerical methods, extending beyond the theoretical scope of this paper. The remainder of this paper, therefore, concentrates on the analysis of AFRs.

C. Important properties of aliasing-free regions

We can now establish properties of the AFR which strengthen our framework and are helpful in manipulating it in subsequent sections.

We begin by extending a classical FF result to the NF regime. Using the modeling (23) of the spatial band, we formulate below Theorem 1, which states that no aliasing arises in the discrete-space AF for any pair $\tilde{\mathbf{x}}, \mathbf{x}$ as soon as the half-wavelength spacing between antennas is maintained. In the FF regime, which permits no range resolution from the steering signal, this principle reduces to its standard angular

interpretation, guaranteeing no angular grating lobes with a half-wavelength antenna spacing.

Theorem 1. Given $z_i := \nu(i\Delta)$ denoting the i -th antenna's locations from the grid \mathcal{Z}_G , if

$$\|z_{i+1} - z_i\| \leq \frac{\lambda_c}{2} \quad (26)$$

is met for all $i \in \{1, \dots, N-1\}$, then the AFR is \mathbb{R}^d for all \mathbf{x} . As a result, any $\mathcal{X} \subseteq \mathbb{R}^d$ is an ASOD.

As previously discussed, this theorem does not imply, neither in FF nor in NF, that the continuous and discrete AFRs, $A(\tilde{\mathbf{x}}, \mathbf{x})$ and $A_S(\tilde{\mathbf{x}}, \mathbf{x})$, can be identical. Instead, it supports that using $K(\tilde{\mathbf{x}}, \mathbf{x})$ to define the soft band limit yields a NF modeling of aliasing artifacts that matches the conventional FF modeling of the grating lobes.

Besides its theoretical reach, the sufficient condition of Theorem 1 can be impractical to effectively design XL-arrays. By extending the array dimensions while increasing carrier frequencies, engineers face physical constraints that prevent meeting a half-wavelength spacing in some applications [8]–[10]. This further motivates the role of our framework, focused on deriving aliasing-safe operating domains, given $\Delta > \lambda_c/2$.

While finding practical expressions for the AFRs is sometimes challenging, we can bound it by another one that is easier to compute. This principle, which we exploit in Section V, is formalized by Properties 1 and 2.

Property 1 (Inclusion principle I). *Two arrays resulting from the sampling of \mathcal{P} with respective sampling steps $\Delta_1 \leq \Delta_2$ yield respective AFRs, $\mathcal{S}_1(\mathbf{x})$ and $\mathcal{S}_2(\mathbf{x})$ that satisfy*

$$\mathcal{S}_2(\mathbf{x}) \subseteq \mathcal{S}_1(\mathbf{x}). \quad (27)$$

for all $\mathbf{x} \in \mathbb{R}^d$

Proof. Since $\Delta_1 \leq \Delta_2$, the condition in (24) is softer when using the sampling step Δ_1 rather than Δ_2 . Thus any $\tilde{\mathbf{x}} \in \mathcal{S}_2(\mathbf{x})$ also meets $\tilde{\mathbf{x}} \in \mathcal{S}_1(\mathbf{x})$. \square

Property 2 (Inclusion principle II). *Given two arrays resulting from the sampling of, respectively, \mathcal{P}_1 and \mathcal{P}_2 , with the same sampling step Δ , the inclusion*

$$\mathcal{P}_1 \subseteq \mathcal{P}_2, \quad (28)$$

implies that their respective AFRs, $\mathcal{S}_1(\mathbf{x})$ and $\mathcal{S}_2(\mathbf{x})$ satisfy

$$\mathcal{S}_2(\mathbf{x}) \subseteq \mathcal{S}_1(\mathbf{x}), \quad (29)$$

for all $\mathbf{x} \in \mathbb{R}^d$.

Proof. Given (28), $K_2(\tilde{\mathbf{x}}, \mathbf{x})$ is the solution of a relaxed version of the maximization problem (23) that yields $K_1(\tilde{\mathbf{x}}, \mathbf{x})$. Therefore, for all $\tilde{\mathbf{x}}, \mathbf{x}$, we have $K_2(\tilde{\mathbf{x}}, \mathbf{x}) \geq K_1(\tilde{\mathbf{x}}, \mathbf{x})$. Consequently

$$K_2(\tilde{\mathbf{x}}, \mathbf{x}) \leq 2\pi\Delta^{-1} \Rightarrow K_1(\tilde{\mathbf{x}}, \mathbf{x}) \leq 2\pi\Delta^{-1}. \quad (30)$$

This directly proves (29) by definition of the AFR. \square

While Property 1 states that densifying the array with extra antennas improves (widens) the AFRs, Property 2 implies that extending the size of the array deteriorates (narrows)

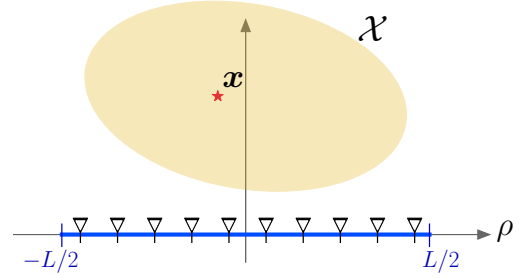


Fig. 6. Schematic representation of a ULA operating in the NF regime.

the AFRs. Conversely, we deduce that truncating an antenna array can only *widen* its AFRs. This possibly counterintuitive conclusion stems from the fact that aliasing artifacts alter the AF as soon as *one* local spatial frequency is greater than $2\pi\Delta^{-1}$. Extending the array only provides more opportunities for this condition to be met in at least one location in the array. This contrasts with the natural intuition from the FF regime, where the matched signal maintains a constant local spatial frequency along the array. In that case, extending the array has no consequence on the aliasing, but solely improves the system's resolution. Similarly, in the NF regime, narrower arrays are not universally preferable since large arrays also offer enhanced spatial resolution for beam pointing. A fundamental trade-off therefore follows between the resolution and the ambiguities caused by aliasing artifacts. Additionally, while wider arrays exhibit aliasing artifacts closer to \mathbf{x} in the AF, their amplitude, which remains to be evaluated, might be lower. This motivates future studies addressing aliasing not only by presence, but also by amplitude.

Finally, while the above properties affect AFRs, Property 3 extends their conclusions to ASODs.

Property 3 (Inclusion principle III). *When two arrays are providing AFRs such that*

$$\mathcal{S}_2(\mathbf{x}) \subseteq \mathcal{S}_1(\mathbf{x}) \quad (31)$$

holds for all $\mathbf{x} \in \mathbb{R}^d$, any operating domain \mathcal{X} that is an ASOD for the array “2”, is also an ASOD for the array “1”.

Proof. Combining the definition (25) with (31), we obtain that if \mathcal{X} is an ASOD for the array “2”, then for all $\mathbf{x} \in \mathcal{X}$, we have $\mathcal{X} \subseteq \mathcal{S}_2(\mathbf{x}) \subseteq \mathcal{S}_1(\mathbf{x})$. \square

The next two sections present applications of the different steps of our methodology to two canonical array topologies, *i.e.*, the ULA and the UCA.

V. UNIFORM LINEAR ARRAY THE NF REGIME

Using the theoretical framework presented in the previous sections, we further develop the specific case of a ULA. Without loss of generality, we consider the zero-centered and horizontal ULA, similar to the toy example used in Section III. Its geometry, shown in Figure 6, is trivially described with $\nu(\rho) = [\rho, 0]^\top$ for $\rho \in \mathcal{P}_L := [-L/2, L/2]$, where L denotes its length.

Following the steps given in Section IV-B, this section derives the expression of the soft band limit, which we denote

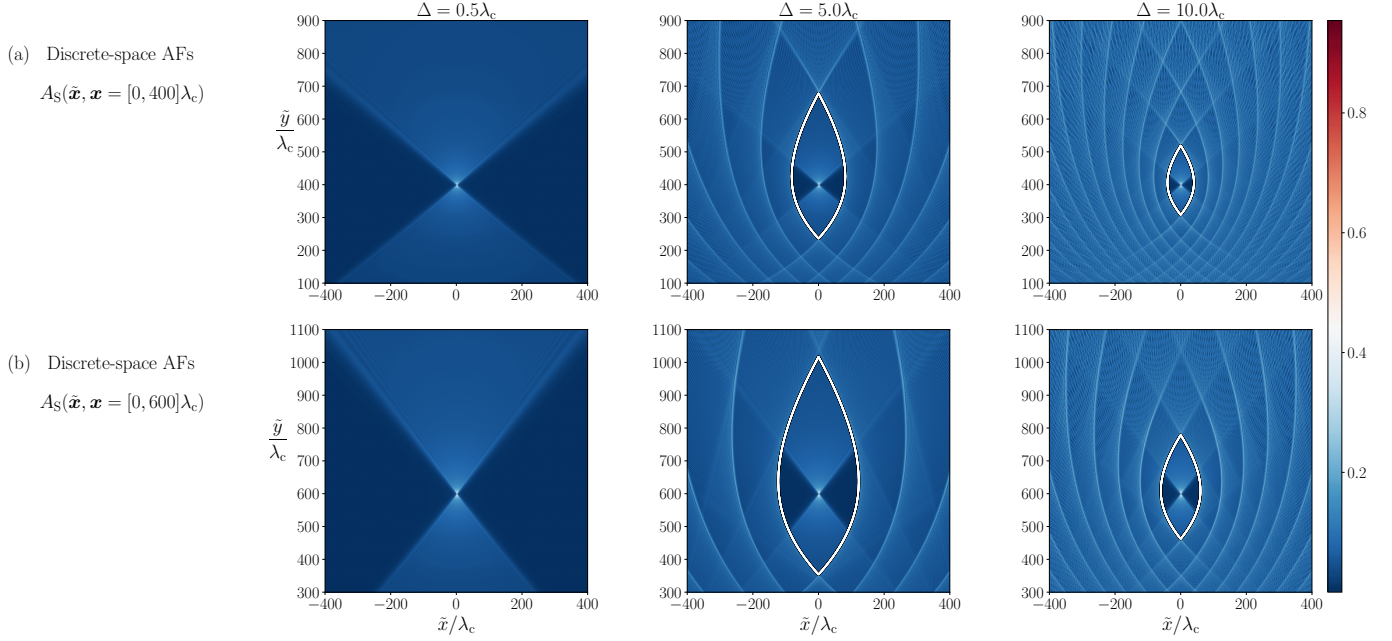


Fig. 7. Discrete-space AFs obtained for a horizontal ULA of length $L = 1000\lambda_c$. (a) with $\mathbf{x} = [0, 400]\lambda_c$ and (b) with $\mathbf{x} = [0, 600]\lambda_c$. The white eye depicts the contour line where $K_\infty(\tilde{\mathbf{x}}, \mathbf{x}) = 2\pi\Delta^{-1}$, i.e., $\partial\mathcal{S}_\infty(\mathbf{x})$, increasing in size as the distance y increases and shrinking as Δ increases.

here by $K_L(\tilde{\mathbf{x}}, \mathbf{x})$, and then deduces the structure of the corresponding AFR, denoted by $\mathcal{S}_L(\mathbf{x})$. Whereas our preliminary work in [25] proposed an approximation of $K_L(\tilde{\mathbf{x}}, \mathbf{x})$, whose validity was limited by the scope of the Fresnel approximation, the current paper derives its exact expression.

We deduce from Property 2 the relevance of studying the aliasing structure of the *infinite-length* ULA as a *worst-case reference*. Indeed, this property guarantees

$$\mathcal{S}_\infty(\mathbf{x}) \subseteq \mathcal{S}_L(\mathbf{x}), \quad (32)$$

for all finite length L . As a result, $\mathcal{S}_\infty(\mathbf{x})$ provides a pessimistic representation of the AFR. Moreover, since $\mathcal{P}_\infty = \mathbb{R}$, the resulting unconstrained computation (23) of the soft band limit is simplified.

For these reasons, we begin this section by applying our methodology to the infinite ULA. We also investigate under which conditions the inclusion (32) is tight with equality. Those are the cases where finite-size ULAs behave as infinite in terms of grating lobes. Next, we provide the general expression of $K_L(\tilde{\mathbf{x}}, \mathbf{x})$, for $L < \infty$, and study the geometry of the resulting AFR, $\mathcal{S}_L(\mathbf{x})$. We finally highlight that our results meet the seminal angular aliasing pattern when pushed to FF regime.

A. Infinite-length ULA

Let us now derive the closed-form expression of the infinite-length ULA's band limit, $K_\infty(\tilde{\mathbf{x}}, \mathbf{x})$ for all 2D locations,

$$\mathbf{x} = [x, y]^\top \quad \text{and} \quad \tilde{\mathbf{x}} = [\tilde{x}, \tilde{y}]^\top, \quad (33)$$

in the upper half-plane ($y > 0$ and $\tilde{y} > 0$). By symmetry, our conclusions directly extend to the other half-plane.

This band limit's expression is formalized in Theorem 2, which is proven in Appendix B. Interestingly, it is entirely driven by two scalar variables

$$u := \left(\frac{\tilde{y}}{y}\right)^{\frac{2}{3}} \quad \text{and} \quad v := \frac{\tilde{x} - x}{y}, \quad (34)$$

reducing it from four degrees of freedom to two. To simplify notations, we also set $w := \frac{v}{u^2 - 1}$.

Theorem 2 (Band limit of an infinite-length ULA). *The infinite-length ULA yields a soft band-limit (Definition 1) that is described by the closed-form expression*

$$K_\infty(\tilde{\mathbf{x}}, \mathbf{x}) = k_c \frac{|(u-1)\beta + v|}{\sqrt{u(\beta^2 + 1)}}, \quad (35)$$

where

$$\beta := \text{sign}(w)u\sqrt{(u+1)^{-1} + w^2} - w. \quad (36)$$

Inspecting the expression (35) for specific locations $\tilde{\mathbf{x}}$ that are aligned with the source location \mathbf{x} yields simplifications formulated in Corollaries 1 and 2, proven in Appendix C. These particular cases are similar to the spatial bandwidth expressions obtained in [19].

Corollary 1. *When $\tilde{\mathbf{x}}$ and \mathbf{x} are horizontally aligned, such that $y = \tilde{y}$, the band limit expression (35) is reduced to*

$$K_\infty(\tilde{\mathbf{x}}, \mathbf{x}) = k_c \frac{|v|}{\sqrt{v^2/4 + 1}}. \quad (37)$$

Corollary 2. *When $\tilde{\mathbf{x}}$ and \mathbf{x} are vertically aligned, such that $x = \tilde{x}$, the band limit expression (35) is reduced to*

$$K_\infty(\tilde{\mathbf{x}}, \mathbf{x}) = k_c \frac{|u-1|}{\sqrt{1+u+u^2}}. \quad (38)$$

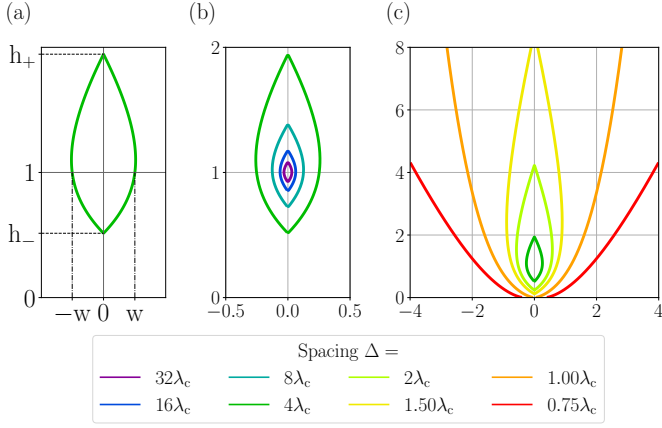


Fig. 8. Geometry of the ULA-eyes. (a) representation of its width w , upper and lower aperture h_+ , h_- . (b)-(c) Examples of ULA-eyes for multiple antenna spacing Δ .

Using Theorem 2, we obtain the AFR of the infinite-length ULA,

$$\mathcal{S}_\infty(\mathbf{x}) = \{\tilde{\mathbf{x}} : K_\infty(\tilde{\mathbf{x}}, \mathbf{x}) \leq 2\pi\Delta^{-1}\}. \quad (39)$$

To illustrate this region, Figure 7 presents numerically computed AFs for long ULAs with $L = 1000\lambda_c$, considering multiple antenna spacings Δ and two distinct source locations \mathbf{x} . Although the simulated arrays have a finite length, the results in Figure 7 are generated in a regime that exactly yields $\mathcal{S}_L(\mathbf{x}) = \mathcal{S}_\infty(\mathbf{x})$, as further explained in Section V-B. We can therefore assume that these long ULAs behave as effectively infinite with respect to the grating lobes.

In that figure, the white eye-shaped contours depict the boundaries $\partial\mathcal{S}_\infty(\mathbf{x})$, computed using the expression (35) in (39). Their apparent correspondence with the actual aliasing front observed in the AFs illustrates that our methodology, based on *local* spatial frequency content of the matched signal, correctly captures the aliasing structure appearing in such AFs.

We now elaborate on the properties of $\mathcal{S}_\infty(\mathbf{x})$. First, we note that $K_\infty(\tilde{\mathbf{x}}, \mathbf{x})$ only depends on u and v . Their definition in (34) translates an x -shift and y -scaling invariance. This effect is detailed in Property 4, which we prove in Appendix D.

Property 4 (Invariance). *Given a spacing Δ , the AFR around the true location \mathbf{x} is identical to the “ULA-eye”, defined as*

$$\mathcal{U} := \mathcal{S}_\infty([0, 1]^\top), \quad (40)$$

up to a translation—centering it in \mathbf{x} — and a rescaling by a factor y . That is,

$$\mathcal{S}_\infty(\mathbf{x}) = y \cdot \mathcal{U} + \begin{bmatrix} \mathbf{x} \\ 0 \end{bmatrix}. \quad (41)$$

Property 4 is an important result enabling us to restrict, without loss of generality, the study of $\mathcal{S}_\infty(\mathbf{x})$ to the one of the “ULA eye” \mathcal{U} , whose sole remaining dependency is with the antenna spacing Δ . Subsequently, we describe the aperture of the eye as a function of Δ in Properties 5 and 6 (also proven in Appendix D).

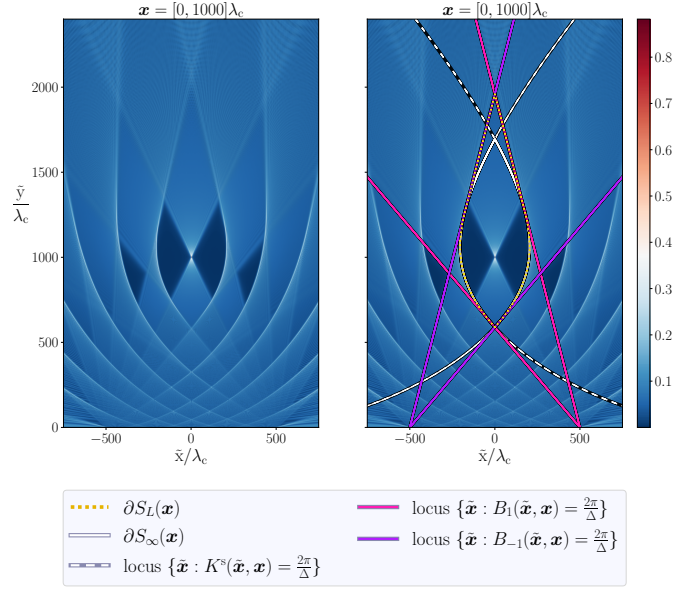


Fig. 9. Ambiguity function $A_S(\tilde{\mathbf{x}}, \mathbf{x} = [0, 1000]\lambda_c)$ for a ULA with length $L = 1000\lambda_c$ and antenna spacing $\Delta = 5\lambda_c$; (left) without annotations and (right) with annotations corresponding to the three regimes of the band limit.

Property 5 (Symmetry). *If $\tilde{\mathbf{x}} \in \mathcal{U}$, then its x -symmetric location $[-\tilde{x}, \tilde{y}]^\top \in \mathcal{U}$.*

Property 6 (Eye’s aperture). *The vertical and horizontal aperture of the ULA eye, characterized by w , h_+ , and h_- as depicted in Figure 8a, are given by*

$$w = \frac{2}{\sqrt{4\delta^2 - 1}} \quad (42)$$

$$h_+ = \begin{cases} \left[\frac{2\delta^2 + 1 + \sqrt{12\delta^2 - 3}}{2(\delta^2 - 1)} \right]^{\frac{3}{2}} & \text{if } \delta > 1 \\ \infty & \text{otherwise} \end{cases}, \quad (43)$$

$$h_- = \begin{cases} \left[\frac{2\delta^2 + 1 - \sqrt{12\delta^2 - 3}}{2(\delta^2 - 1)} \right]^{\frac{3}{2}} & \text{if } \delta > 1 \\ 0 & \text{otherwise} \end{cases}, \quad (44)$$

where

$$\delta = \frac{\Delta}{\lambda_c}. \quad (45)$$

Figures 8b and 8c draw the eyes obtained for multiple antenna spacings Δ . As intuitively understood, and stated in Property 1, increasing this spacing shrinks the eye. Smaller eyes exhibit near vertical-symmetry, while larger ones elongate upward until one reaches spacing such that $\lambda_c/2 < \Delta \leq \lambda_c$. In that case, expressions (43) and (44) saturate, causing the ULA-eye to degenerate. The degenerate eyes (Fig. 8c) never close vertically and are squeezed on the bottom. When $\Delta \leq \lambda_c/2$, the eye no longer has boundaries because, as stated in Theorem 1, we have $\mathcal{U} = \mathbb{R}^2$.

B. Finite-length ULA

When the length L is finite, the expressions for the soft band limit and the resulting AFR become more sophisticated. Theorem 3, proven in Appendix E, provides the composite expression of $K_L(\tilde{\mathbf{x}}, \mathbf{x})$, which exhibits three regimes that we explain in this section.

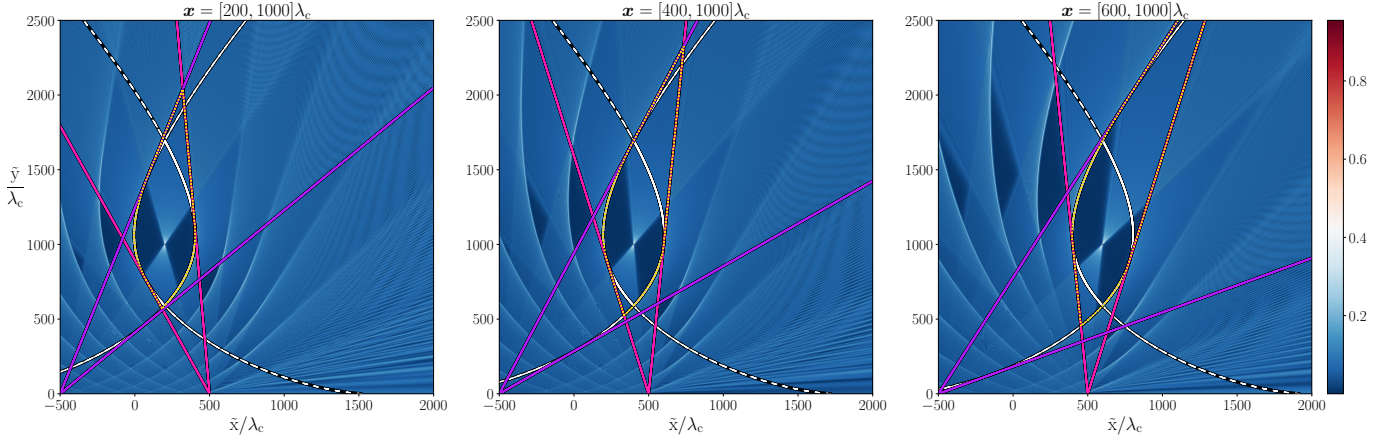


Fig. 10. Ambiguity functions for a ULA with length $L = 1000\lambda_c$ and antenna spacing $\Delta = 5\lambda_c$ for multiple source locations \mathbf{x} that yield distinct AFR shapes, combining the three regimes explained in Section V-B. The legend is identical to Figure 9.

Theorem 3 (Band limit of an finite-length ULA). *The ULA of length L yields a soft band-limit (Definition 1) that is described by the closed-form expression*

$$K_L(\tilde{\mathbf{x}}, \mathbf{x}) = \begin{cases} K_\infty(\tilde{\mathbf{x}}, \mathbf{x}) & \text{if } |y\beta + x| \leq \frac{L}{2} \\ \max\{B_1(\tilde{\mathbf{x}}, \mathbf{x}), K^s(\tilde{\mathbf{x}}, \mathbf{x})\} & \text{if } |y\beta + x| > \frac{L}{2} \\ & \text{and } |y\beta^s + x| \leq \frac{L}{2} \\ \max\{B_1(\tilde{\mathbf{x}}, \mathbf{x}), B_{-1}(\tilde{\mathbf{x}}, \mathbf{x})\} & \text{otherwise} \end{cases}, \quad (46)$$

where

$$B_q(\tilde{\mathbf{x}}, \mathbf{x}) = k_c [\cos(\theta_q(\tilde{\mathbf{x}})) - \cos(\theta_q(\mathbf{x}))], \quad (47)$$

$$K^s(\tilde{\mathbf{x}}, \mathbf{x}) = k_c \frac{|(u-1)\beta^s + v|}{\sqrt{u((\beta^s)^2 + 1)}}, \quad (48)$$

and where, for $q \in \{-1, 1\}$,

$$\theta_q(\mathbf{x}) := \angle(\mathbf{x} - [q \operatorname{sign}(w) \frac{L}{2}, 0]^\top), \quad (49)$$

$$\beta^s := -\operatorname{sign}(w)u\sqrt{(u+1)^{-1} + w^2} - w. \quad (50)$$

The first regime of (46) highlights the equivalence $K_L(\tilde{\mathbf{x}}, \mathbf{x}) = K_\infty(\tilde{\mathbf{x}}, \mathbf{x})$ for all pairs $\tilde{\mathbf{x}}, \mathbf{x}$ such that

$$|y\beta + x| \leq \frac{L}{2}. \quad (51)$$

This can be explained since by construction of Theorem 2's proof (see Appendix B), the variable β is linked to the value of ρ that sees the highest local frequency, through

$$y\beta + x = \arg \max_{\rho \in \mathbb{Z}} |\dot{\xi}(\rho)|. \quad (52)$$

Therefore, under (51), the constraint $\rho \in [-L/2, L/2]$ does not exclude the global maximizer of the unconstrained maximization that underpins $K_\infty(\tilde{\mathbf{x}}, \mathbf{x})$. Corollary 3 directly follows.

Corollary 3. *Consider an infinite-length ULA and its truncation of length L . For a given location \mathbf{x} , if for all $\tilde{\mathbf{x}} \in \mathcal{S}_\infty(\mathbf{x})$ the condition (51) holds, then*

$$\mathcal{S}_L(\mathbf{x}) = \mathcal{S}_\infty(\mathbf{x}). \quad (53)$$

Proof. This is a direct consequence of Theorem 3. \square

Despite the non-trivial expression of β (which depends on both \mathbf{x} and $\tilde{\mathbf{x}}$), we can intuitively anticipate that (51) is typically satisfied when \mathbf{x} and $\tilde{\mathbf{x}}$ are sufficiently close to each other and to the array's center, compared to the length L . Such close-by locations see the array as effectively infinite.

Conversely, when this condition is not met, the band limit expression is mainly driven by its third regime, *i.e.*, $K_L(\tilde{\mathbf{x}}, \mathbf{x}) = \max\{B_1(\tilde{\mathbf{x}}, \mathbf{x}), B_{-1}(\tilde{\mathbf{x}}, \mathbf{x})\}$. The second regime describes the transition between the two others. In the third regime, the highest local frequency occurs at one of the array edges, revealing, in (47), the well-known difference of directional cosines with angles taken relative to the given edge.

Expression (46) can now be exploited to compute $\mathcal{S}_L(\mathbf{x})$. Unlike Figure 7, which focused on the “near-infinite array” regime, Figure 9 shows results with a further source location, causing $\mathcal{S}_L(\mathbf{x}) \neq \mathcal{S}_\infty(\mathbf{x})$. The bottom part of the boundary $\partial\mathcal{S}_L(\mathbf{x})$ matches $\partial\mathcal{S}_\infty(\mathbf{x})$ as it corresponds to locations $\tilde{\mathbf{x}}$ that meets condition (51). The top part, however, is attained in the third regime of the band limit, causing $\partial\mathcal{S}_L(\mathbf{x})$ to instead follow the directional cosine lines (in pink).

In Figure 10, we show similarly annotated AFs for multiple source locations \mathbf{x} , illustrating how the corresponding AFRs vary in shape while consistently adhering to the lines marking the regimes we detailed in this section.

C. Connections with the far-field regime

To conclude our analysis of ULAs, we examine the behavior of our AFR expression as the scenario approaches the FF regime. Figure 11 presents results similar to those in Figure 10, with the source locations \mathbf{x} that are progressively moved further from a ULA of length $200\lambda_c$. The right-side subfigure notably shows the case where \mathbf{x} is in the FF as it reaches the Fraunhofer distance. As the distances become much larger than the array length L , two effects emerge: (i) the “directional cosine” regime becomes the sole active regime in the boundary $\partial\mathcal{S}_L(\mathbf{x})$, and (ii) the cosines in (47) measured from both array edges converge. The combination of these two effects connects our model with the seminal angular repetition, characteristic of the FF regime.

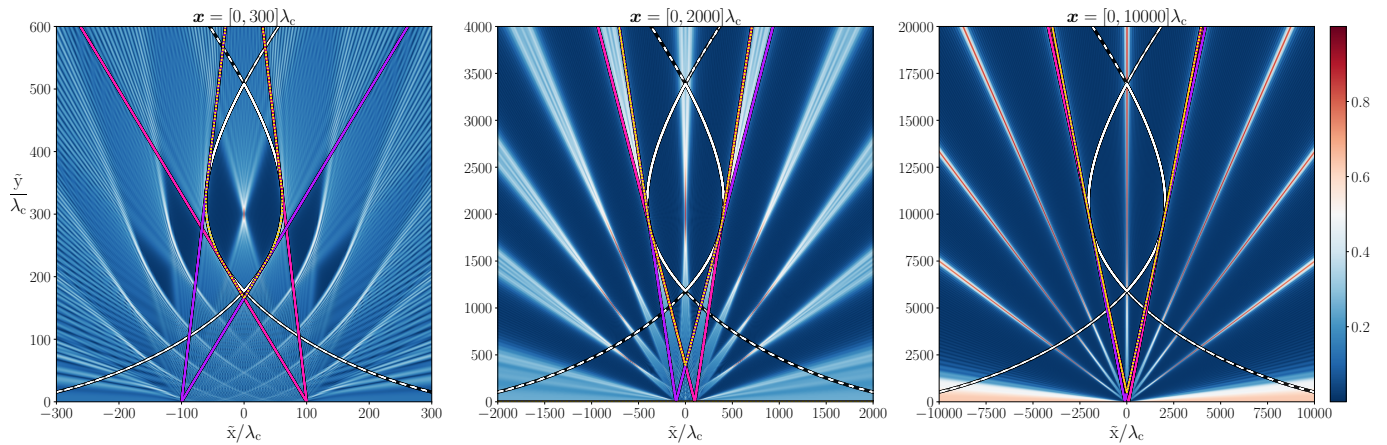


Fig. 11. Ambiguity functions for a ULA with length $L = 200\lambda_c$ and antenna spacing $\Delta = 5\lambda_c$ for multiple source locations \mathbf{x} that progressively tends towards the FF conditions. The location $\mathbf{x} = [0, 10000]\lambda_c$ is in the FF according to the Fraunhofer criterion. The legend is identical to Figure 9.

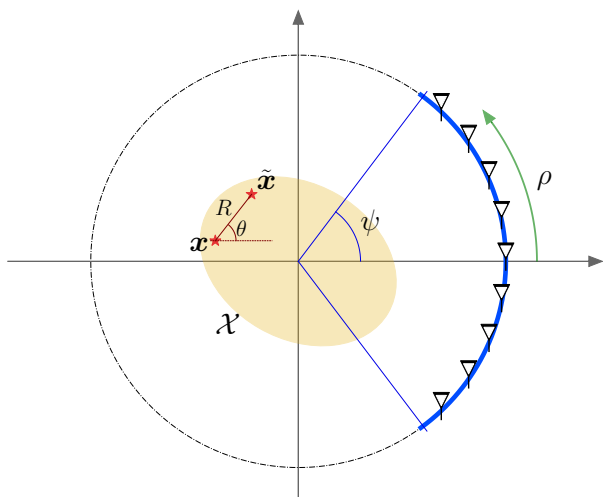


Fig. 12. Schematic representation of a UCA

VI. DISTRIBUTED UNIFORM CIRCULAR ARRAY

Circular arrays constitute a natural reference for theoretical studies on XL-arrays [14], [28], due to their inherent isotropic geometry providing a 360-degree coverage. As such, this topology can be considered as the canonical example of the “perfectly” distributed XL-array. This simple geometry enables the derivation of closed-form expressions, exploiting the Fourier-Bessel series for its associated radiation patterns and ambiguity function, notably demonstrating a resolution with an order of magnitude comparable to the carrier wavelength [14], [25]. While such results are associated with complete circles of continuous antenna elements, we aim here to exploit our framework to understand the aliasing structure that appears in the discrete-space AF of UCAs.

In all generality, a UCA is described by an antenna domain \mathcal{Z} that draws an arc on the zero-centered circle of radius R_{UCA} surrounding the operating domain \mathcal{X} , as shown in Figure 12.

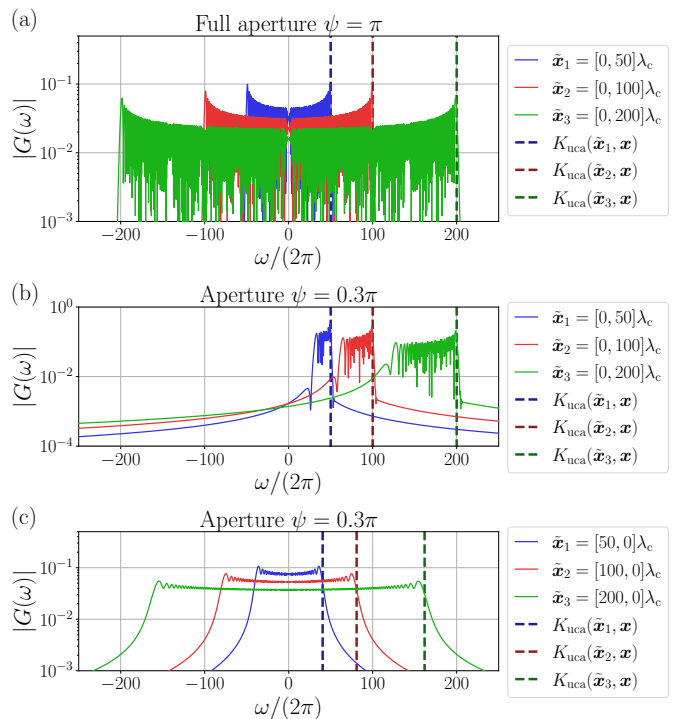


Fig. 13. Spectrum $G(\omega; \tilde{\mathbf{x}}, \mathbf{x} = \mathbf{0})$ for a UCAs with $R_{\text{UCA}} = 10,000\lambda_c$. (a) with $\psi = \pi$. (b) with $\psi = 0.3\pi$ and vertical position differences. (c) with $\psi = 0.3\pi$ and horizontal position differences.

The parametric path variable ρ denotes here an angle such that

$$\nu(\rho) = R_{\text{UCA}} \begin{bmatrix} \cos(\rho) \\ \sin(\rho) \end{bmatrix}, \quad (54)$$

and we set the domain $\mathcal{P} = [-\psi, \psi]$ with $0 \leq \psi \leq \pi$ to enable us to consider either the full circle with $\psi = \pi$ or arcs with $\psi < \pi$. The antenna spacing Δ corresponds, in the context of this section, to an *angular* spacing, expressed in radians.

To develop further the expression of the phase (20), we restrict the focus of this section to an infinitely large array with $R_{\text{UCA}} \rightarrow \infty$ surrounding the operating domain \mathcal{X} . Practically speaking, the resulting study provides good representations of

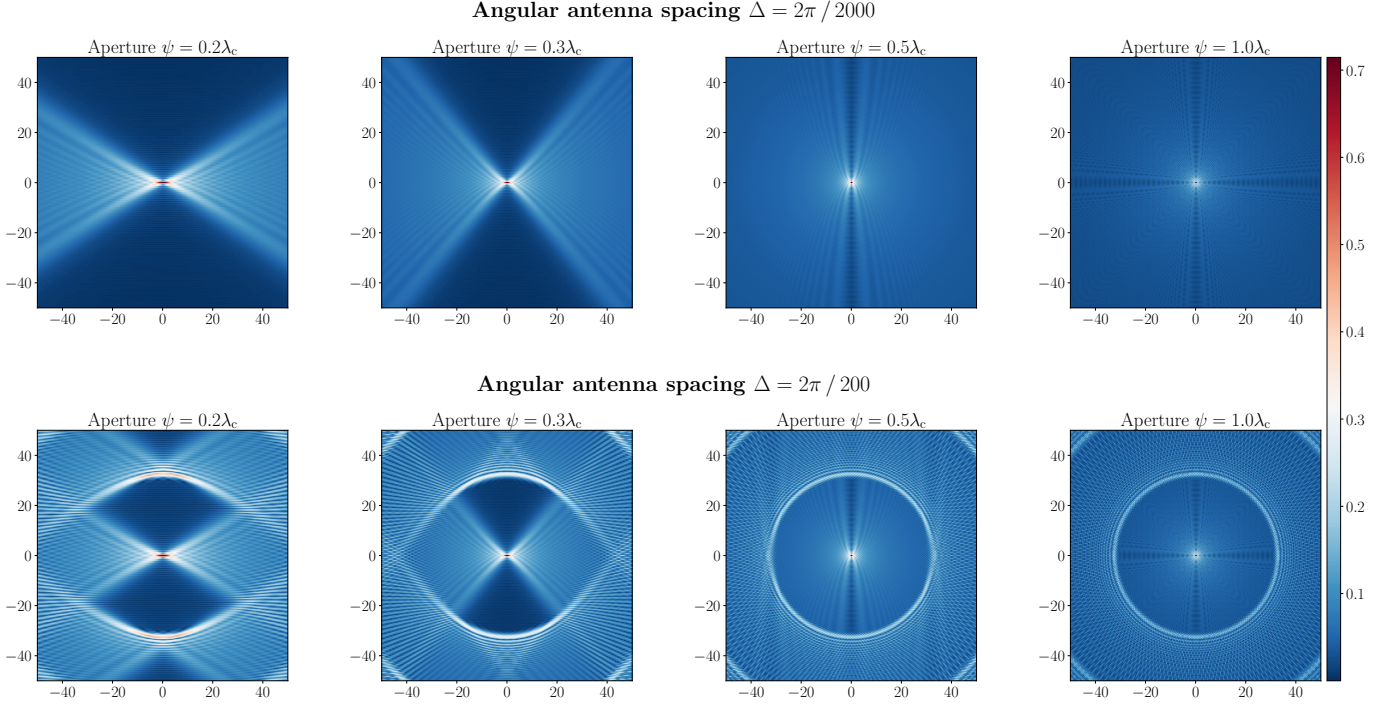


Fig. 14. Discrete-space AFs, $|A_S(\tilde{\mathbf{x}}, \mathbf{x} = \mathbf{0})|$, for a UCA of radius $R_{\text{uca}} = 10,000\lambda_c$ and multiple apertures ψ . (top) uniform angular spacing $\Delta = 2\pi/2000$. (bottom) $\Delta = 2\pi/200$.

the aliasing structure one observes for a non-infinite radius satisfying

$$R_{\text{uca}} \gg \max\{\|\mathbf{x}\| : \mathbf{x} \in \mathcal{X}\}. \quad (55)$$

Under the infinite-radius condition, the matched signal's amplitude, given in (19), is asymptotically constant, causing $G_\alpha(\omega)$ to be a Dirac delta. As a result, $G(\omega; \tilde{\mathbf{x}}, \mathbf{x})$ and $G_\xi(\omega)$ are exactly equals, up to a constant coefficient.

The phase of this signal, given in (20), remains non-linear across the infinite circle \mathcal{Z} , hence preserving the NF nature of this scenario. However, in the reciprocal point of view, each specific antenna's location $\mathbf{z} = \nu(\rho)$ is seen in the FF of the domain \mathcal{X} . Said differently, the domain \mathcal{X} is infinitely small compared to the distance separating it from \mathbf{z} . Consequently, this condition validates the modeling in [14], implying that for all $\mathbf{z} \in \mathcal{Z}$ and all $\tilde{\mathbf{x}}, \mathbf{x} \in \mathcal{X}$, the matched signal phase reads

$$\xi(\rho) = k_c R \cos(\rho - \theta), \quad (56)$$

where we define

$$R := \|\mathbf{x} - \tilde{\mathbf{x}}\| \text{ and } \theta := \angle(\mathbf{x} - \tilde{\mathbf{x}}), \quad (57)$$

as visualized in Figure 12. The resulting band limit is straightforwardly obtained and formalized in Theorem 4.

Theorem 4. *The infinite-radius UCA yields a soft band limit (Definition 1) that is described by the closed-form expression*

$$K_{\text{uca}}(\tilde{\mathbf{x}}, \mathbf{x}) = k_c R \Omega(\theta), \quad (58)$$

where $\Omega(\theta)$ is the visual aperture of the array at the angle θ . We define it as

$$\Omega(\theta) := \max_{\rho \in [-\psi, \psi]} |\sin(\rho - \theta)|. \quad (59)$$

Proof. Using (56), the local spatial frequency is trivially expressed as $\xi(\rho) = -k_c R \sin(\rho - \theta)$. Developing the definition (23) with this expression directly provides (58). \square

Let us note that (59) possesses a closed-form expression that we provide here for the sake of clarity. If there is an integer n such that

$$|\theta + (2n + 1)\frac{\pi}{2}| \in [-\psi, \psi], \quad (60)$$

then the visual aperture takes its maximum value $\Omega(\theta) = 1$. Otherwise, the constraints in (59) are active, implying that

$$\Omega(\theta) = \max\{|\sin(\psi + \theta)|, |\sin(\psi - \theta)|\}. \quad (61)$$

Fig. 13 shows how expression (58) of the band limit properly captures the spectrum $G(\omega; \tilde{\mathbf{x}}, \mathbf{x})$ given a UE located in $\mathbf{x} = \mathbf{0}$, and multiple tested locations $\tilde{\mathbf{x}}$. The complete UCA with $\psi = \pi$ exhibits an angular invariance, implying only symmetric spectra, as seen in Figure 13. This invariance no longer holds for incomplete circles. Therefore, it results in asymmetric spatial spectra (Figure 13b), except for the particular case of horizontal positional difference $\tilde{\mathbf{x}} - \mathbf{x}$ (Figure 13c), assuming an array oriented as depicted in Figure 12.

We can now study the resulting AFR of the UCA, given the angular spacing Δ . It follows the interpretable expression:

$$\mathcal{S}_{\text{uca}}(\mathbf{x}) := \{\tilde{\mathbf{x}} : K_{\text{uca}}(\tilde{\mathbf{x}}, \mathbf{x}) = 2\pi\Delta^{-1}\} \quad (62)$$

$$= \left\{ (R, \theta) : R \geq \frac{\lambda_c}{\Delta\Omega(\theta)} \right\}. \quad (63)$$

Expression (63) informs us that the aliasing front appears around \mathbf{x} , in each direction θ , at a distance $\frac{\lambda_c}{\Delta\Omega(\theta)}$. Interestingly, as soon as the UCA draws a *half-circle*, i.e., when $\psi \geq \frac{\pi}{2}$, condition (60) is met, and hence the visual aperture

provides its maximum value $\Omega(\theta) = 1$ for all θ . As a result, the aliasing front draws a perfect circle around \mathbf{x} .

By contrast, when $\psi < \frac{\pi}{2}$, then $\Omega(\theta) = 1$ only for angles satisfying (60). These are angles such that the line passing through \mathbf{x} that is normal to them crosses the array. In other angles, the visual aperture follows (61), resulting in a locally linear aliasing front in the AF.

These effects can be observed in Figure 14, which shows discrete-space AFs computed for UCAs with multiple apertures λ_c and either $\Delta = (2\pi)/2000$ or $\Delta = (2\pi)/200$ as angular antenna spacing. The denser array acts as the aliasing-free reference. We indeed observe a circular aliasing front of radius $\frac{\lambda_c}{\Delta} = 31.83\lambda_c$ with alternating fronts and decaying zones repeating at every multiple of this radius. This pattern aligns with the analysis we presented in Figure 4. When $\psi < \frac{\pi}{2}$, the circle stretches as the visual aperture increases. The portion of the front that fits the circle exactly corresponds to the angular aperture of the array (*i.e.*, an arc of 2ψ radians). These two arcs—upper and lower—are oriented perpendicularly to the array. Notably, the resulting eye-shaped region always includes the full-aperture disc, in accordance with Property 2. That is, because any arc of aperture 2ψ inherently represents a truncation of the whole circle.

VII. CONCLUSIONS

This paper proposed a theoretical framework to address the challenging characterization of near field (NF) grating lobes, which we interpreted as aliasing artifacts affecting ambiguity functions (AFs). By leveraging a local spatial-frequency representation of the steering and matched signals, we described the structural origin of these aliasing artifacts. Our framework then exploits this understanding and provides a systematic methodology to derive aliasing-free regions (AFRs), which formally defines the geometry drawn by the NF grating lobes. Studying these regions is the key to designing aliasing-safe operating domain (ASOD), guaranteeing no aliasing when restricting the array's operation in this domain. Deriving methods to mathematically determine ASODs therefore constitutes the direct next step expected to follow the current work. This paper illustrated its practical value in deriving closed-form expressions of AFRs for both uniform linear arrays (ULAs) and uniform circular arrays (UCAs).

Importantly, our framework is currently restricted to explaining the geometrical presence of NF grating lobes. As a key feature of the NF regime, these lobes are usually weaker than the main lobe, which allows extremely large-scale arrays (XL-arrays) to theoretically function beyond the AFR. Expanding our framework to aliasing amplitudes is therefore critical to study the reachable performance in this context. Similarly, subsequent work extending our framework to capture the resolution of both the main and grating lobes would constitute a key step toward a comprehensive characterization of the AF's properties.

Future work directions also include exploiting the flexibility of our approach to determine the AFRs for more sophisticated array topologies that meet the demands of practical applications. Finally, we note that our methodology is adaptable

to study the coupled space-time-frequency AFs arising when considering wideband systems and Doppler effects.

ACKNOWLEDGMENTS

L. Defraigne and B. Sambon thank the FRIA and the FRS-FNRS for their financial support

AUTHOR CONTRIBUTIONS

G. Monnoyer and L. Vandendorpe came to the idea of investigating the impact of array discretization on the ambiguity function through the approach of spatial frequencies, and the formal link between AF and spectral content. G. Monnoyer introduced the AFR and ASOD notions. G. Monnoyer achieved the theoretical results for the ULA. L. Vandendorpe derived the results for the UCA. All numerical results were generated by G. Monnoyer, as well as the first version of the manuscript. All co-authors highly contributed to the ordering of ideas, the identification of the best ways to present them, and to the improvement of the text.

COMPETING INTERESTS

There are no competing interests to declare.

APPENDIX

A. Proof of Theorem 1

The first-order derivative of (20) is given by

$$\dot{\xi}(\rho) = k_c \left(\frac{\nu(\rho) - \tilde{\mathbf{x}}}{\|\nu(\rho) - \tilde{\mathbf{x}}\|} - \frac{\nu(\rho) - \mathbf{x}}{\|\nu(\rho) - \mathbf{x}\|} \right) \dot{\nu}(\rho). \quad (64)$$

Using the Cauchy-Schwarz inequality, we conclude that

$$|\dot{\xi}(\rho)| \leq k_c \left\| \frac{\nu(\rho) - \tilde{\mathbf{x}}}{\|\nu(\rho) - \tilde{\mathbf{x}}\|} - \frac{\nu(\rho) - \mathbf{x}}{\|\nu(\rho) - \mathbf{x}\|} \right\| \|\dot{\nu}(\rho)\|. \quad (65)$$

The first factor in the right-side product in (65) is the norm of a difference of two unit-norm vectors, which is upper-bounded by 2. As a result, $K(\tilde{\mathbf{x}}, \mathbf{x}) \leq 2k_c \max_{\rho \in \mathcal{P}} \|\dot{\nu}(\rho)\|$ for any pair $\tilde{\mathbf{x}}, \mathbf{x}$. Since $k_c = \frac{2\pi}{\lambda_c}$, the condition (24) is always met when

$$\Delta \max_{\rho \in \mathcal{P}} \|\dot{\nu}(\rho)\| \leq \frac{\lambda_c}{2}. \quad (66)$$

Finally, from the mean-value theorem, for any pair $\rho_1, \rho_2 \in \mathcal{P}$, we have

$$\|\nu(\rho_2) - \nu(\rho_1)\| \leq |\rho_2 - \rho_1| \max_{\rho \in \mathcal{P}} \|\dot{\nu}(\rho)\|. \quad (67)$$

Therefore, (26) validates the condition in the definition of the AFR for all $\tilde{\mathbf{x}}, \mathbf{x} \in \mathbb{R}^d$, from which we directly conclude that any set $\mathcal{X} \subseteq \mathbb{R}^d$ is an ASOD. This concludes this proof.

B. Proof of Theorem 2

Particularizing Definition 1 to the infinite-length ULA described in Section V yields

$$K_\infty(\tilde{\mathbf{x}}, \mathbf{x}) := \max_{\rho \in \mathbb{Z}} |\dot{\xi}(\rho)|. \quad (68)$$

Developing the expression of $\dot{\xi}(\rho)$ with the above locations leads to

$$\dot{\xi}(\rho) = k_c \left[\frac{\rho - x}{((\rho - x)^2 + y^2)^{\frac{1}{2}}} - \frac{\rho - \tilde{x}}{((\rho - \tilde{x})^2 + \tilde{y}^2)^{\frac{1}{2}}} \right], \quad (69)$$

and its derivative is

$$\ddot{\xi}(\rho) = k_c \left[\frac{y^2}{((\rho - x)^2 + y^2)^{\frac{3}{2}}} - \frac{\tilde{y}^2}{((\rho - \tilde{x})^2 + \tilde{y}^2)^{\frac{3}{2}}} \right]. \quad (70)$$

Since we assume $y > 0$ and $\tilde{y} > 0$ (excluding the source to be located inside and behind the antenna array), the function $\dot{\xi}(\rho)$ in (69) is continuous as both denominators are always non-zero. A direct application of the L'Hospital's rule shows that this function tends toward 0 in both $-\infty$ and $+\infty$. Therefore, the maximizer of (68) is necessarily given by (one of) the roots of $\dot{\xi}(\rho)$. Denoting this maximizer by $\bar{\rho}$, we have

$$K_\infty(\tilde{\mathbf{x}}, \mathbf{x}) = |\dot{\xi}(\bar{\rho})|. \quad (71)$$

Since $\bar{\rho}$ is one root of $\dot{\xi}(\rho)$, it must satisfy

$$\tilde{y}^{\frac{4}{3}}((\bar{\rho} - x)^2 + y^2) = y^{\frac{4}{3}}((\bar{\rho} - \tilde{x})^2 + \tilde{y}^2). \quad (72)$$

Before solving (72), let us simplify its expression by introducing the normalization

$$\beta := \frac{\bar{\rho} - x}{y}, \quad (73)$$

and by exploiting the notations introduced in (34). After a few algebraic manipulations, we rewrite (72) as

$$(\beta - v)^2 + u^3 = u^2(\beta^2 + 1). \quad (74)$$

The above defines a second-order polynomial in β , whose roots are

$$\beta = \frac{qu\sqrt{(u^2 - 1)(u - 1) + v^2} - v}{u^2 - 1}. \quad (75)$$

for $q \in \{-1, 1\}$. The above square root's content is always positive since $u > 0$ under our conditions.

Since (73) amounts to write $\bar{\rho} = y\beta + x$, we must now evaluate $\dot{\xi}(y\beta + x)$ and determine the sign of q that yields maximality. To this end, let us first similarly apply the notations introduced in (34) and (73) in order to repress (69). With a few algebraic manipulations, we obtain

$$\dot{\xi}(y\beta + x) = k_c \left[\frac{\beta}{(\beta^2 + 1)^{\frac{1}{2}}} - \frac{\beta - v}{((\beta - v)^2 + u^3)^{\frac{1}{2}}} \right], \quad (76)$$

Now substituting the identity (74) in (76) enables the simplification

$$\dot{\xi}(y\beta + x) = k_c \frac{(u - 1)\beta + v}{u(\beta^2 + 1)^{\frac{1}{2}}}. \quad (77)$$

Exploiting (71), we conclude that there is at least one sign q such that

$$K_\infty(\tilde{\mathbf{x}}, \mathbf{x}) = |\dot{\xi}(y\beta + x)| = k_c \left| \frac{(u - 1)\beta + v}{u(\beta^2 + 1)^{\frac{1}{2}}} \right| \quad (78)$$

$$= k_c \frac{|(u - 1)\beta + v|}{u(\beta^2 + 1)^{\frac{1}{2}}}, \quad (79)$$

which is exactly (35).

The next step of this proof is to find the sign q that maximizes $|\dot{\xi}(y\beta + x)|$. To this end, we use (75) to develop (78). Proceeding separately for the numerator and the denominator, we have

$$(u - 1)\beta + v = \frac{u}{u + 1} (q\sqrt{(u^2 - 1)(u - 1) + v^2} + v), \quad (80)$$

and

$$\beta^2 + 1 = \frac{1}{u^2 - 1} ((u^2 - 1)(u^3 - 1) + v^2(u^2 + 1) - 2quv\sqrt{(u^2 - 1)(u - 1) + v^2}). \quad (81)$$

Reminding that $u > 0$, we conclude that the numerator and denominator of (78) are respectively maximized and minimized, in absolute value, when $q = \text{sign}(v)$, thereby guaranteeing that this sign maximizes $|\dot{\xi}(y\beta + x)|$. Injecting this sign in (75) and applying the change of variable $v = (u^2 - 1)w$ yields (36) and concludes this proof.

C. Proofs of Corollaries 1 and 2

proof of corollary 1. Starting from (74) with $u = 1$, we have

$$(\beta - v)^2 + 1 = \beta^2 + 1, \quad (82)$$

which simplifies to $\beta = v/2$ (and thus the maximizer is $\bar{\rho} = yv/2 + x$). The expression (35) therefore simplifies into (37), concluding this proof. \square

proof of corollary 2. When $v = w = 0$, the expression (36) is reduced to

$$\beta = \text{sign}(w)u/\sqrt{u + 1}. \quad (83)$$

The expression (35) is in turns reduced to

$$K_\infty(\tilde{\mathbf{x}}, \mathbf{x}) = \frac{u}{\sqrt{u+1}} \sqrt{1 + \frac{u^2}{u+1}}, \quad (84)$$

which simplifies into (38), concluding this proof. \square

D. Proofs of ULA's Aliasing-free Regions Properties

Proof of Property 4. Let us consider the pair of $\tilde{\mathbf{x}}_1 = [\tilde{x}_1, \tilde{y}_1]^\top$, $\mathbf{x}_1 = [0, 1]^\top$, from which we construct another as $\tilde{\mathbf{x}}_2 = [y_2\tilde{x}_1 + x_2, y_2\tilde{y}_1]^\top$, $\mathbf{x}_2 = [x_2, y_2]^\top$. This construction always yields

$$K_\infty(\tilde{\mathbf{x}}_1, \mathbf{x}_1) = K_\infty(\tilde{\mathbf{x}}_2, \mathbf{x}_2) \quad (85)$$

because both pairs give rise to the same values for u and v . Therefore for all $\tilde{\mathbf{x}}_1 \in \mathcal{S}_\infty(\mathbf{x}_1)$, the second pair meets $\tilde{\mathbf{x}}_2 \in \mathcal{S}_\infty(\mathbf{x}_2)$, and inversely. By construction the equality $\mathcal{S}_\infty(\mathbf{x}_1) = \mathcal{U}$ holds. Since we can also write

$$\tilde{\mathbf{x}}_2 = y_2 \cdot \tilde{\mathbf{x}}_1 + \begin{bmatrix} x_2 \\ 0 \end{bmatrix}, \quad (86)$$

it concludes the proof. \square

Proof of Property 5. Since \mathcal{U} is obtained from Theorem 2 with $x = 0$ and $y = 1$, inverting the sign of \tilde{x} inverts the sign of v and hence also inverts the sign of β , while maintaining their absolute value. Therefore, both the numerator and the denominator in (35) are unchanged in absolute value. It results in

$$K_\infty([-\tilde{x}, \tilde{y}]^\top, [0, 1]^\top) = K_\infty([\tilde{x}, \tilde{y}]^\top, [0, 1]^\top), \quad (87)$$

for all $\tilde{\mathbf{x}}$. Therefore, given $\mathbf{x} = [0, 1]^\top$ if $[\tilde{x}, \tilde{y}]^\top$ satisfies (39), then $[-\tilde{x}, \tilde{y}]^\top$ satisfies it too. \square

Proof of Property 6. We begin this proof with the expression (42) of the width w . Starting from (37), we have that the boundary of $\mathcal{S}_\infty(\mathbf{x})$ is met in that direction when $\delta|v| = \sqrt{v^2/4 + 1}$, which is trivially met when $v = 2/\sqrt{4\delta^2 - 1}$. Note that in the context of the eye \mathcal{U} , we have $v = \tilde{x}$, thereby proving (42).

We now prove the vertical apertures using (38). Similarly, the boundary of $\mathcal{S}_\infty(\mathbf{x})$ is found when $\delta|u - 1| = \sqrt{1 + u + u^2}$. Squaring both sides yields

$$\Delta^2(u^2 - 1)^2 = 1 + u + u^2, \quad (88)$$

which finds a solution in

$$u = \frac{2\delta^2 + 1 + q\sqrt{12\delta^2 - 3}}{2(\delta^2 - 1)}, \quad (89)$$

for $q \in \{-1, 1\}$. When $\delta^2 = 1$, then (88) finds 0 as its only solution. When $\frac{3}{4} \leq \delta^2 < 1$, then (88) finds only negative solutions which must be excluded because Theorem 2 is only valid for positive u (upper half plane only). When $\delta^2 < \frac{3}{4}$, the polynomial equation (88) finds no real solution. In all those cases, the eye's aperture vertically degenerates in 0 (on the bottom) and $+\infty$ (on top). Otherwise, the solution with $q = 1$ gives the top border and the one with $q = -1$, the lower border. Finally, noticing that, in the context of the eye \mathcal{U} , we have $u = \tilde{y}^{\frac{2}{3}}$ leads to (43) and (44), which concludes this proof. \square

E. Proof of Theorem 3

This proof follows that of Theorem 2 and uses the same notations. We aim to solve

$$K_L(\tilde{\mathbf{x}}, \mathbf{x}) := \max_{\rho \in [-\frac{L}{2}, \frac{L}{2}]} |\dot{\xi}(\rho)|. \quad (90)$$

When the unconstrained maximizer, $y\beta + x$, is in $[-\frac{L}{2}, \frac{L}{2}]$, it is also the maximizer of (90), thereby demonstrating the first case in (46).

When the constraint excludes $y\beta + x$, the solution can either be given by the only other local extremum of $\dot{\xi}(\rho)$ or by evaluating it at one edge of the constraint. That is, since we showed in Theorem 2's proof that $\dot{\xi}(\rho)$ is continuous, tends to 0 when $\rho \mapsto \pm\infty$, and possesses at most two local extrema, in $y\beta + x$ and $y\beta^s + x$. This situation can be separated into two cases, respectively providing the second and third regimes in (46).

case $y\beta^s + x \in [-\frac{L}{2}, \frac{L}{2}]$: As $\dot{\xi}(\rho)$ tends to 0 when $\rho \mapsto \pm\infty$, this case necessarily implies that $|\dot{\xi}(y\beta^s + x)| > |\dot{\xi}(-\text{sign}(w)\frac{L}{2})|$. The two remaining candidates to maximize (90) are therefore $\rho = y\beta^s + x$ and $\rho = \text{sign}(w)\frac{L}{2}$. Evaluating $|\dot{\xi}(\cdot)|$ in these values provides, after a few algebraic manipulations, the expressions of $B_1(\tilde{\mathbf{x}}, \mathbf{x})$ and $K^s(\tilde{\mathbf{x}}, \mathbf{x})$, respectively given in (47) and (48)

case "otherwise": In that case, the only candidates to maximize (90) are the two edges of the array, i.e., $\rho = \pm\frac{L}{2}$, which directly yields $K_L(\tilde{\mathbf{x}}, \mathbf{x}) = \max\{B_1(\tilde{\mathbf{x}}, \mathbf{x}), B_{-1}(\tilde{\mathbf{x}}, \mathbf{x})\}$ and concludes this proof.

REFERENCES

- [1] X. Li, Z. Dong, Y. Zeng, S. Jin, and R. Zhang, "Near-Field Beam Focusing Pattern and Grating Lobe Characterization for Modular XL-Array," in *GLOBECOM 2023 - 2023 IEEE Global Communications Conference*, Dec. 2023, pp. 4068–4073, iSSN: 2576-6813.
- [2] H. Chen, M. F. Keskin, A. Sakhnini, N. Decarli, S. Pollin, D. Dardari, and H. Wymeersch, "6G Localization and Sensing in the Near Field: Features, Opportunities, and Challenges," *IEEE Wireless Communications*, vol. 31, no. 4, pp. 260–267, 2024.
- [3] O. T. Demir, E. Bjornson, and L. Sanguineti, "Foundations of User-Centric Cell-Free Massive MIMO," *SIG*, vol. 14, no. 3-4, pp. 162–472, Jan. 2021.
- [4] Z. Wu and L. Dai, "Multiple Access for Near-Field Communications: SDMA or LDMA?" *IEEE Journal on Selected Areas in Communications*, vol. 41, no. 6, pp. 1918–1935, Jun. 2023.
- [5] A. Sakhnini, S. De Bast, M. Guenach, A. Bourdoux, H. Sahli, and S. Pollin, "Near-Field Coherent Radar Sensing Using a Massive MIMO Communication Testbed," *IEEE Transactions on Wireless Communications*, vol. 21, no. 8, pp. 6256–6270, Aug. 2022.
- [6] Z. Wang, J. Zhang, H. Du, W. E. I. Sha, B. Ai, D. Niyato, and M. Debbah, "Extremely Large-Scale MIMO: Fundamentals, Challenges, Solutions, and Future Directions," *IEEE Wireless Communications*, vol. 31, no. 3, pp. 117–124, Jun. 2024.
- [7] Y. Liu, Z. Wang, J. Xu, C. Ouyang, X. Mu, and R. Schober, "Near-Field Communications: A Tutorial Review," *IEEE Open Journal of the Communications Society*, vol. 4, pp. 1999–2049, 2023.
- [8] H. Lu, Y. Zeng, C. You, Y. Han, J. Zhang, Z. Wang, Z. Dong, S. Jin, C.-X. Wang, T. Jiang, X. You, and R. Zhang, "A Tutorial on Near-Field XL-MIMO Communications Toward 6G," *IEEE Communications Surveys & Tutorials*, vol. 26, no. 4, pp. 2213–2257, 2024.
- [9] H. Lu and Y. Zeng, "How Does Performance Scale with Antenna Number for Extremely Large-Scale MIMO?" in *ICC 2021 - IEEE International Conference on Communications*, Jun. 2021, pp. 1–6, iSSN: 1938-1883.
- [10] V. C. Rodrigues, A. Amiri, T. Abrão, E. de Carvalho, and P. Popovski, "Low-Complexity Distributed XL-MIMO for Multiuser Detection," in *2020 IEEE International Conference on Communications Workshops (ICC Workshops)*, Jun. 2020, pp. 1–6, iSSN: 2474-9133.
- [11] C. Zhou, C. You, H. Zhang, L. Chen, and S. Shi, "Sparse Array Enabled Near-Field Communications: Beam Pattern Analysis and Hybrid Beamforming Design," *IEEE Transactions on Wireless Communications*, pp. 1–1, 2025.
- [12] A. Kosasih, O. T. Demir, N. Kolomvakis, and E. Bjornson, "Spatial Frequencies and Degrees of Freedom: Their roles in near-field communications," *IEEE Signal Processing Magazine*, vol. 42, no. 1, pp. 33–44, Jan. 2025.
- [13] R. Gui, B. Huang, W.-Q. Wang, and Y. Sun, "Generalized Ambiguity Function for FDA Radar Joint Range, Angle and Doppler Resolution Evaluation," *IEEE Geoscience and Remote Sensing Letters*, vol. 19, pp. 1–5, 2022.
- [14] L. Vandendorpe, L. Defraigne, G. Thiran, T. Poirion, and C. Craeye, "Positioning and transmission in cell-free networks: ambiguity function, and MRC/MRT array gains," in *ICASSP 2025 - 2025 IEEE International Conference on Acoustics, Speech and Signal Processing (ICASSP)*, Apr. 2025, pp. 1–5.
- [15] L. Zhuang and X. Liu, "Coherent synthesis sparse aperture radar with grating lobes suppressed using frequency MIMO technique," in *2008 IEEE Radar Conference*, May 2008, pp. 1–5, iSSN: 2375-5318.

- [16] Y. V. Krivosheev and A. V. Shishlov, "Grating lobe suppression in phased arrays composed of identical or similar subarrays," in *2010 IEEE International Symposium on Phased Array Systems and Technology*, Oct. 2010, pp. 724–730.
- [17] Z. Gao, Z. Wan, D. Zheng, S. Tan, C. Masouros, D. W. K. Ng, and S. Chen, "Integrated Sensing and Communication With mmWave Massive MIMO: A Compressed Sampling Perspective," *IEEE Transactions on Wireless Communications*, vol. 22, no. 3, pp. 1745–1762, Mar. 2023.
- [18] H. Zhang, C. s. You, and C. Zhou, "Near-field Beam Focusing under Discrete Phase Shifters," in *2025 IEEE Wireless Communications and Networking Conference (WCNC)*, Mar. 2025, pp. 1–6, iSSN: 1558-2612.
- [19] L. Ding, E. G. Ström, and J. Zhang, "Degrees of Freedom in 3D Linear Large-Scale Antenna Array Communications—A Spatial Bandwidth Approach," *IEEE Journal on Selected Areas in Communications*, vol. 40, no. 10, pp. 2805–2822, Oct. 2022.
- [20] L. Ding, J. Zhang, and E. G. Ström, "Spatial Bandwidth Asymptotic Analysis for 3D Large-Scale Antenna Array Communications," *IEEE Transactions on Wireless Communications*, vol. 23, no. 4, pp. 2638–2652, Apr. 2024.
- [21] A. Kosasih, O. T. Demir, N. Kolomvakis, and E. Bjornson, "Spatial Frequencies and Degrees of Freedom: Their roles in near-field communications," *IEEE Signal Processing Magazine*, vol. 42, no. 1, pp. 33–44, Jan. 2025.
- [22] A. Swindlehurst and T. Kailath, "Passive direction-of-arrival and range estimation for near-field sources," in *Fourth Annual ASSP Workshop on Spectrum Estimation and Modeling*, Aug. 1988, pp. 123–128.
- [23] W. Qiu, W. Wang, and W. Xiao, "DOA Estimation of Near-field Passive Sources with Acoustic Array Based on Fractional Fourier Transform," in *OCEANS 2018 MTS/IEEE Charleston*, Oct. 2018, pp. 1–4.
- [24] M. Jian, A. Tang, Y. Chen, and Y. Zhao, "Fractional Fourier Transformation Based XL-MIMO Near-Field Channel Analysis," in *2024 IEEE 25th International Workshop on Signal Processing Advances in Wireless Communications (SPAWC)*, Sep. 2024, pp. 221–225.
- [25] G. Monnoyer, L. Defraigne, B. Sambon, J. Louveaux, and L. Vandendorpe, "Chirp-Based Aliasing Analysis of Arrays in the Spherical Wavefront Regime," May 2025, arXiv:2505.05378 [eess].
- [26] T. Abhayapala, R. Kennedy, and R. Williamson, "Spatial Aliasing for Nearfield Sensor Arrays," *Electronics Letters*, Aug. 2002.
- [27] E. Chassande-Mottin and P. Flandrin, "On the stationary phase approximation of chirp spectra," in *Proceedings of the IEEE-SP International Symposium on Time-Frequency and Time-Scale Analysis (Cat. No.98TH8380)*, Oct. 1998, pp. 117–120.
- [28] S. Häfner, M. Käske, and R. Thomä, "On Calibration and Direction Finding with Uniform Circular Arrays," *International Journal of Antennas and Propagation*, vol. 2019, no. 1, p. 1523469, 2019.